# Supplementary Information

# Atomic-scale regulation of anionic and cationic migration in alkali metal batteries

Pan Xiong[1,2,#], Fan Zhang[2,#], Xiuyun Zhang[3,#], Yifan Liu[1], Yunyan Wu[1], Shijian Wang[2], Javad Safaei[2], Bing Sun[2], Renzhi Ma[4], Zongwen Liu[5], Yoshio Bando[4], Takayoshi Sasaki[4], Xin Wang[1], Junwu Zhu[1*], Guoxiu Wang[2*]

[1]Key Laboratory for Soft Chemistry and Functional Materials of Ministry Education, Nanjing University of Science and Technology, Nanjing, 210094, China

[2]Centre for Clean Energy Technology, School of Mathematical and Physical Sciences, University of Technology Sydney, NSW 2007, Australia

[3]College of Physical Science and Technology, Yangzhou University, Yangzhou, 225002, China

[4]International Center for Materials Nanoarchitectonics (WPI-MANA), National Institute for Materials Science (NIMS), Namiki 1-1, Tsukuba, Ibaraki, 305-0044, Japan
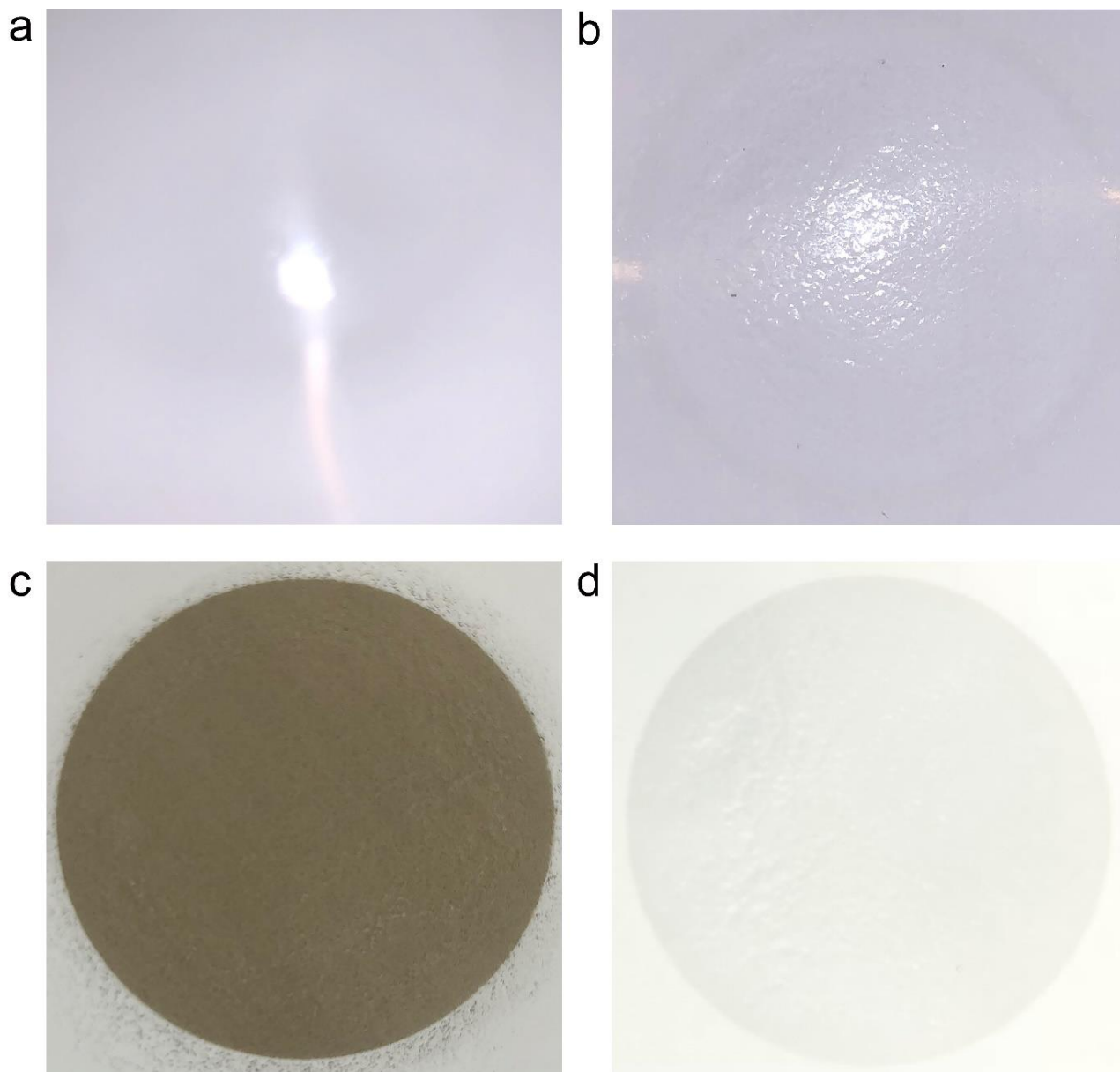
[5]School of Chemical and Biomolecular Engineering, The University of Sydney, NSW 2006, Australia

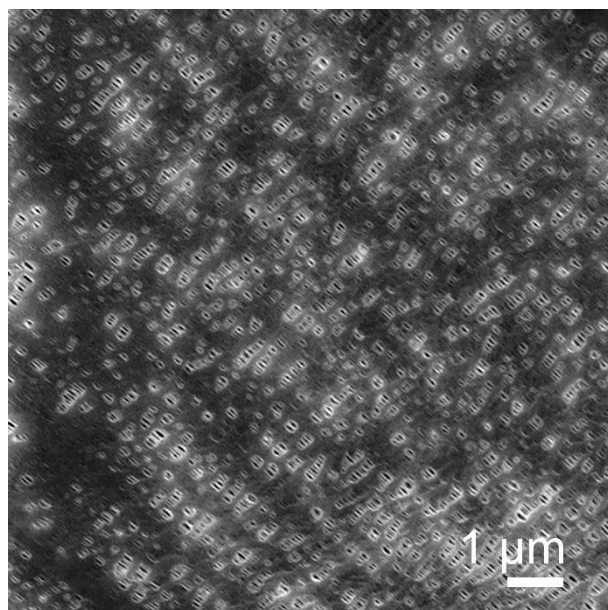[#]These authors contributed equally: Pan Xiong, Fan Zhang, Xiuyun Zhang
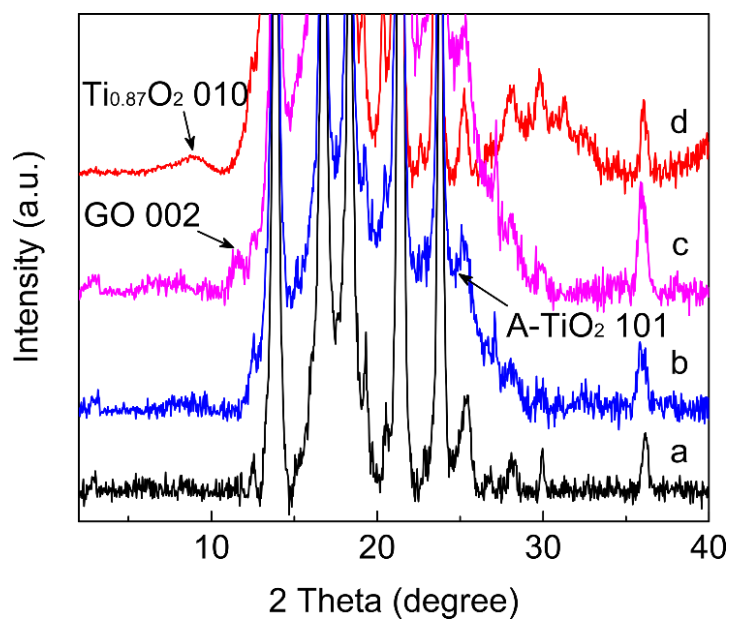
[*]e-mail: zhujw@njust.edu.cn; guoxiu.wang@uts.edu.au
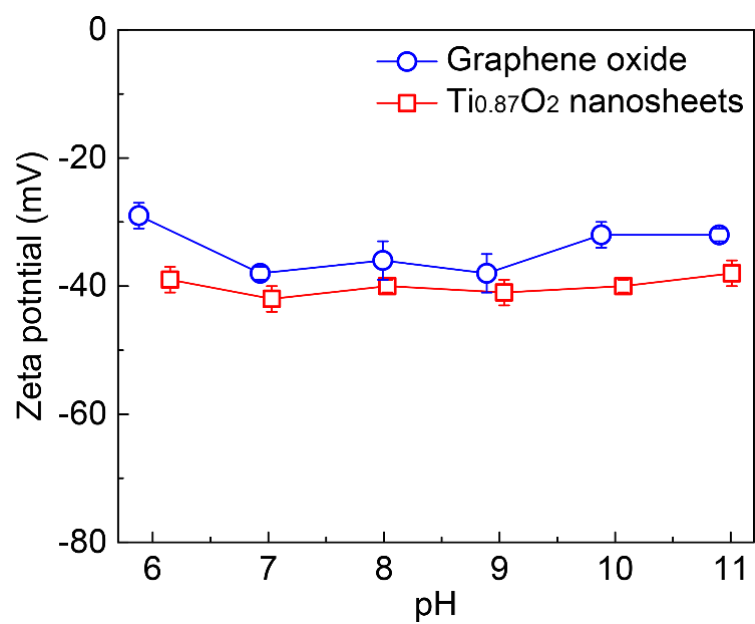
**Supplementary Figure 1.** Zeta-potentials of the suspensions of graphene oxide and $Ti_{0.87}O_2$ nanosheets.

**Supplementary Figure 2.** Photographs of the (a) PP, (b) anatase $TiO_2$/PP, (c) GO/PP, and (d) $Ti_{0.87}O_2$/PP separators.
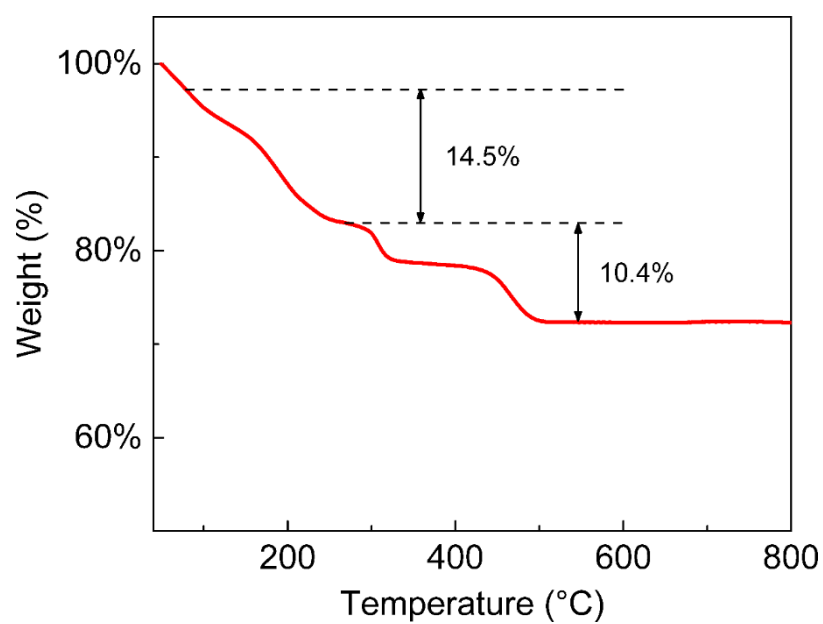
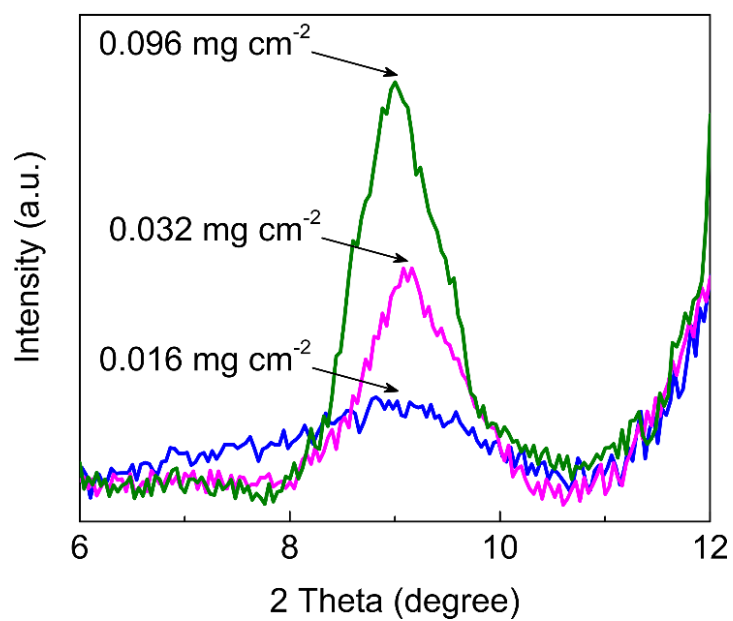**Supplementary Figure 3.** SEM image of the commercial PP separators.

**Supplementary Figure 4.** XRD patterns of (a) PP, (b) anatase $TiO_2$/PP, (c) GO/PP, and (d) $Ti_{0.87}O_2$/PP

separators. The 101 diffraction peak of anatase $TiO_2$ (A-$TiO_2$), 002 diffraction peak of GO and 010

diffraction peak of $Ti_{0.87}O_2$ were marked.
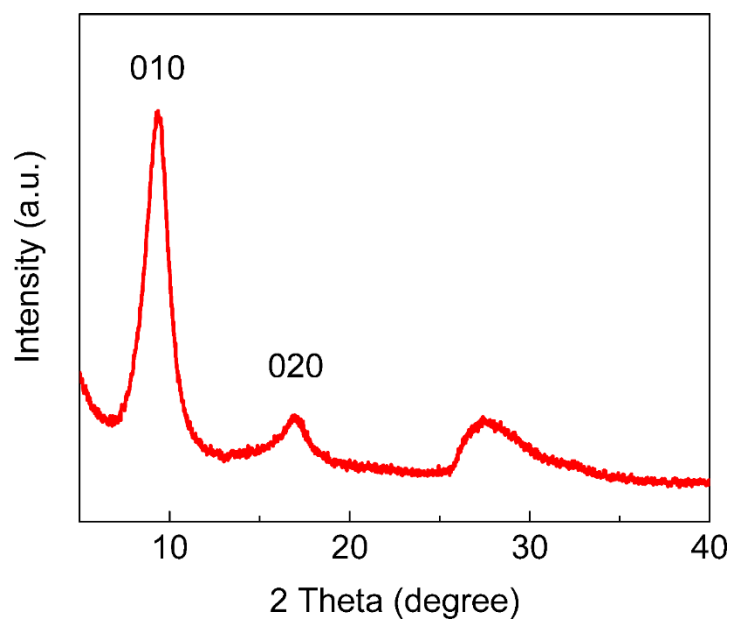
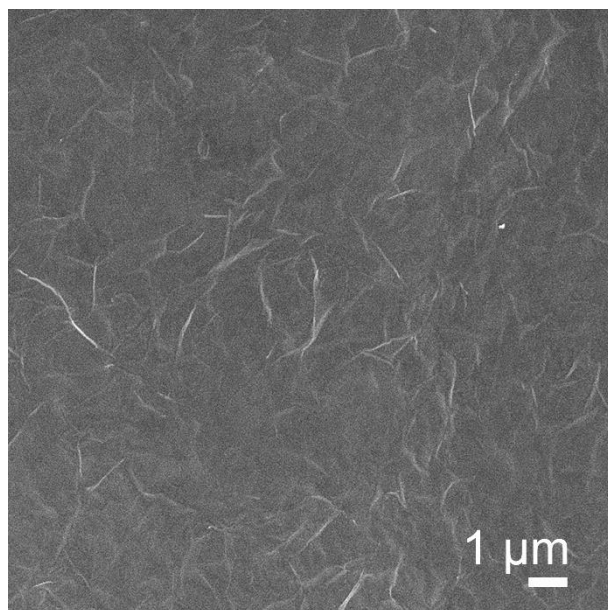**Supplementary Figure 5.** XRD pattern for the $Ti_{0.87}O_2$ nanosheets without PP separators.

**Supplementary Figure 6.** Thermogravimetric curve for the nanosheet films without PP separators.

**Supplementary Figure 7.** XRD patterns of $Ti_{0.87}O_2$/PP separators with different surface area mass loadings.

**Supplementary Figure 8.** SEM image of $Ti_{0.87}O_2$/PP separators with a surface area mass loading of 0.032 mg cm$^{-2}$.
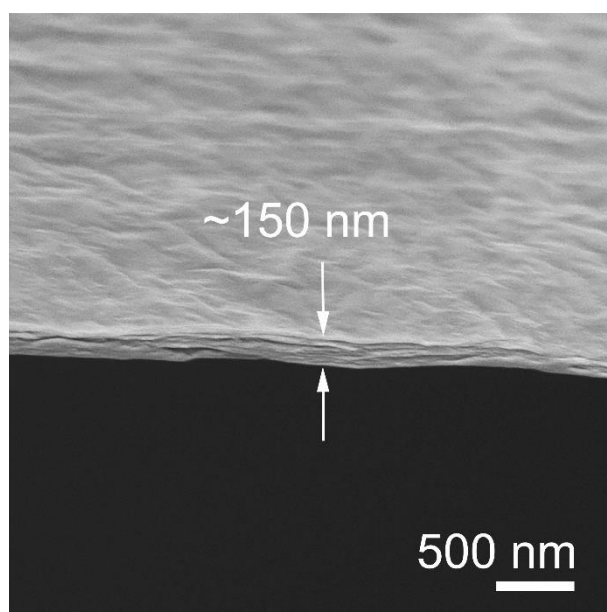
**Supplementary Figure 9.** Cross-section SEM image of $Ti_{0.87}O_2$/PP separators with a surface area mass

loading of 0.032 mg cm$^{-2}$.
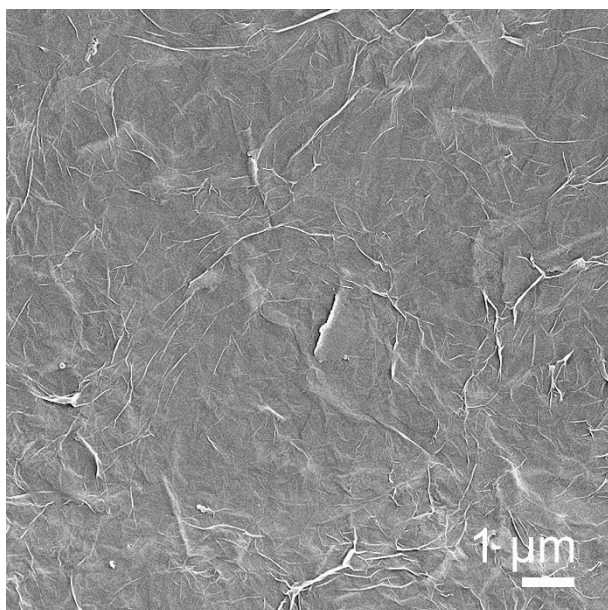
**Supplementary Figure 10.** SEM image of $Ti_{0.87}O_2$/PP separators with a surface area mass loading of 0.096 mg cm$^{-2}$.

**Supplementary Figure 11.** Cross-section SEM image of $Ti_{0.87}O_2$/PP separators with a surface area mass loading of 0.096 mg cm$^{-2}$.

**Supplementary Figure 12.** SEM image of anatase $TiO_2$/PP separators with a surface area mass loading
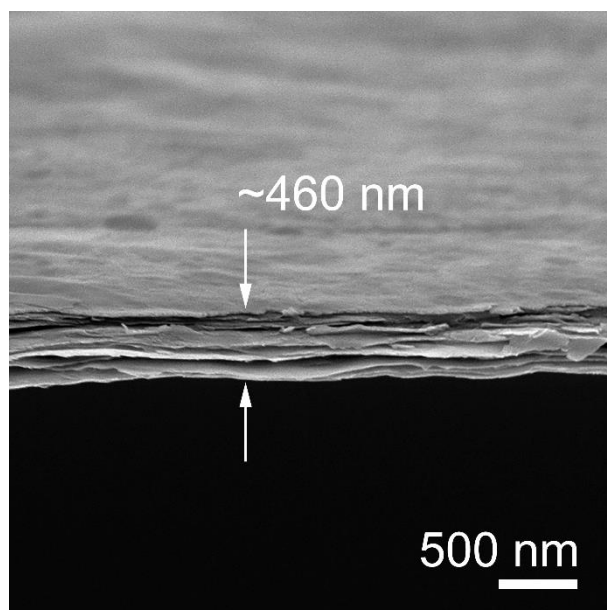
of 0.016 mg cm$^{-2}$.

**Supplementary Figure 13.** SEM image of GO/PP separators with a surface area mass loading of 0.016 mg cm$^{-2}$.
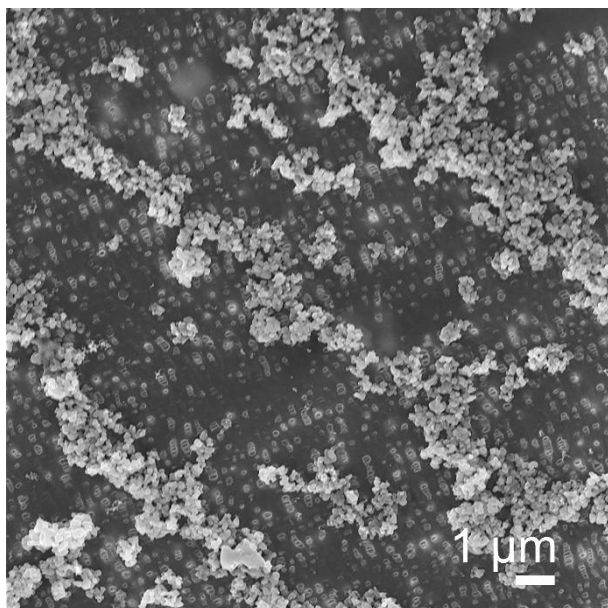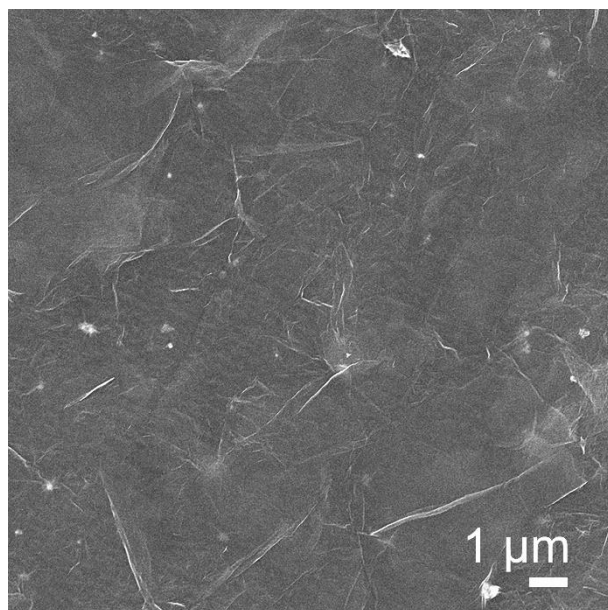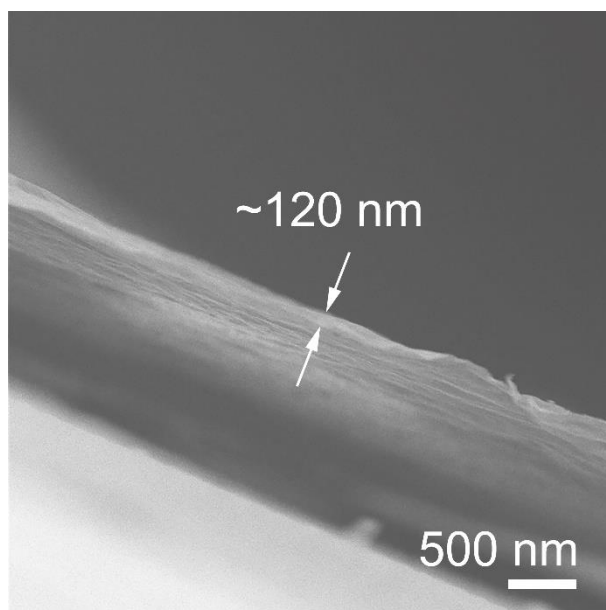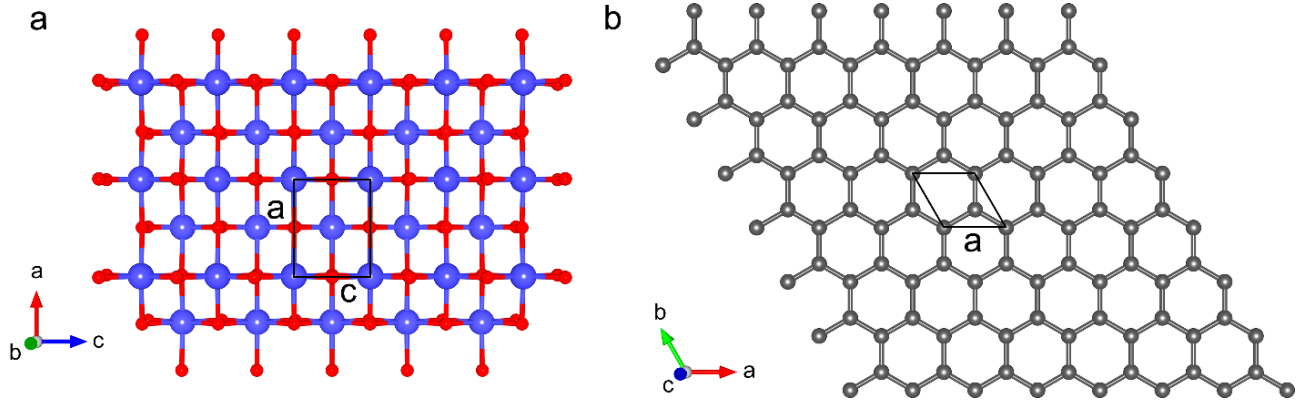
**Supplementary Figure 14.** Cross-section SEM image of GO/PP separators with a surface area mass loading of 0.016 mg cm$^{-2}$.

**Supplementary Figure 15.** 2D theoretical specific surface area of $Ti_{0.87}O_2$ and GO monolayers. (a) In-plane structure of $Ti_{0.87}O_2$ with a rectangular unit cell: $a$ = 0.38 nm and $c$ = 0.30 nm. (b) In-plane structure of graphene with a hexagonal unit cell: $a$ = 0.25 nm. The ideal graphene structure was used to estimate the 2D theoretical specific surface area of GO. For an approximate calculation, the single layers of $Ti_{0.87}O_2$ and graphene were assumed to neatly deposit on the PP separator without gap. The 2D theoretical specific surface area of $Ti_{0.87}O_2$ single layer can be calculated based on the in-plane unit cell area, $W_{(Ti0.87O2)} = 2 M_{(Ti0.87O2)} / (a \times c \times N_A)$. The 2D theoretical specific surface area of GO single layer can be calculated based on the in-plane unit cell area, $W_{(GO)} = 2 M_{(C)} / (a \times a \times \sin 120° \times N_A)$. $N_A$ is the Avogadro's number, $M_{(Ti0.87O2)}$ and $M_{(C)}$ are the formula weights of $Ti_{0.87}O_2$ and carbon. Under a same specific surface area, $W_{(GO)} \times n_{(GO)} = W_{(Ti0.87O2)} \times n_{(Ti0.87O2)}$. $n_{(GO)}$ and $n_{(Ti0.87O2)}$ are the number of single layers of GO and $Ti_{0.87}O_2$, respectively. So, the $n_{(GO)} / n_{(Ti0.87O2)}$ = ~2.9. Considering the crystallinity thickness of GO and $Ti_{0.87}O_2$ is 0.34 and 0.75 nm, respectively. The thickness ($h$) of the functional layer of GO and $Ti_{0.87}O_2$ with the same specific surface area is $h_{(GO)} / h_{(Ti0.87O2)}$ = ~1.36.
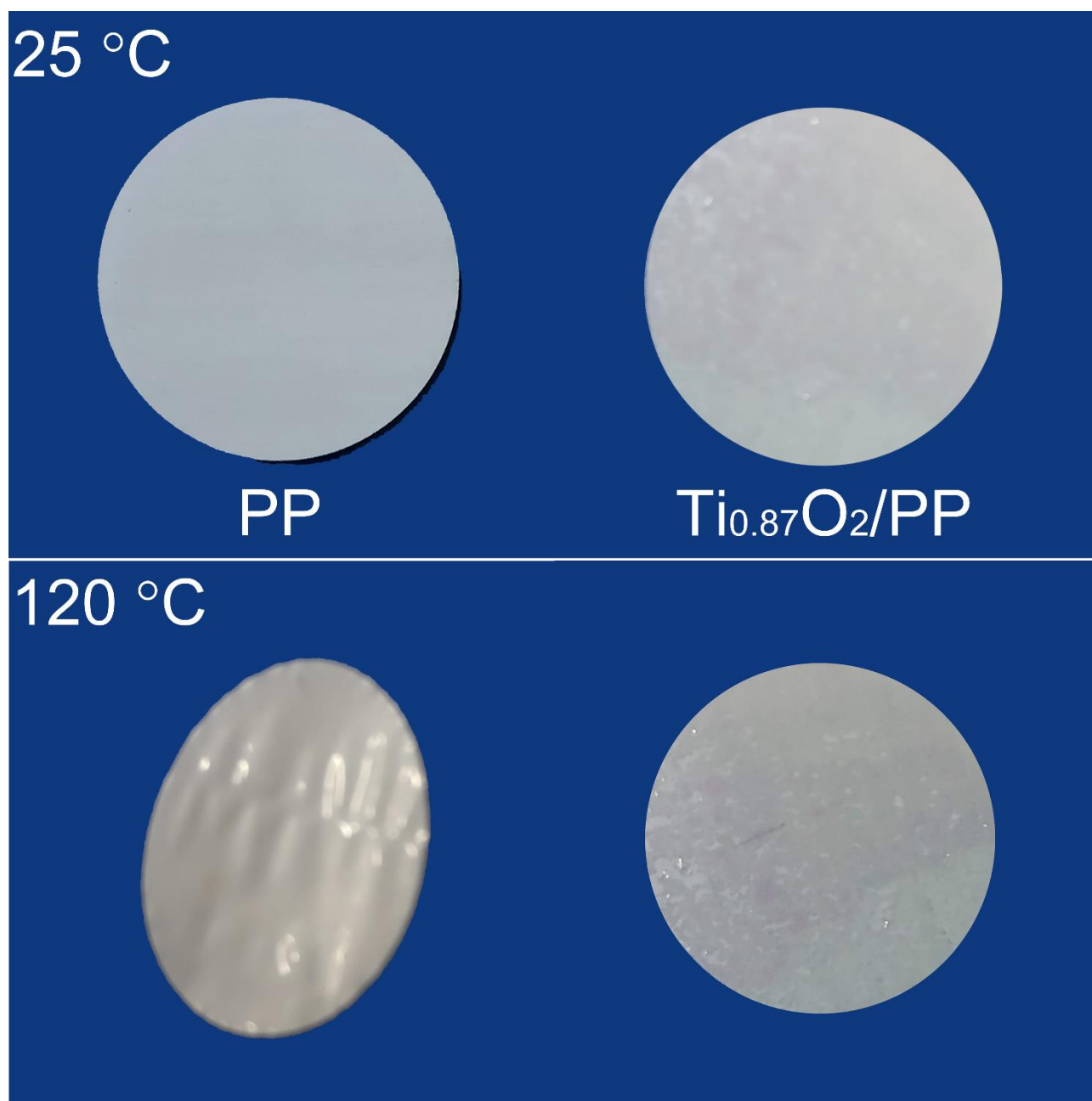
**Supplementary Figure 16.** Photographic pictures of the PP and $Ti_{0.87}O_2$/PP separators before and after heating process.
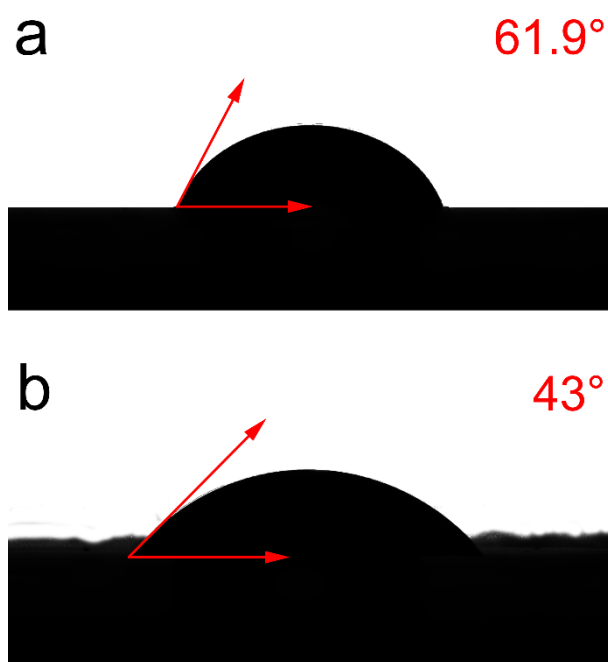
**Supplementary Figure 17.** Contact angle measurements for electrolytes (1 M LiTFSI in DME: DOL

1: 1, v/v) on (a) PP and (b) $Ti_{0.87}O_2$/PP separators.

**Supplementary Figure 18.** Digital photos of the $Ti_{0.87}O_2$/PP separator under different bending conditions.
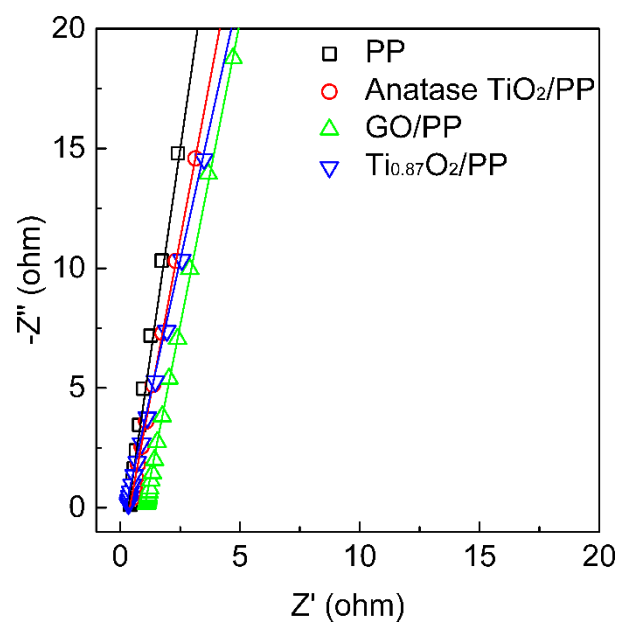
**Supplementary Figure 19.** Nyquist plots of PP, anatase $TiO_2$/PP, GO/PP and $Ti_{0.87}O_2$/PP separators estimating the Li-ion conductivity.
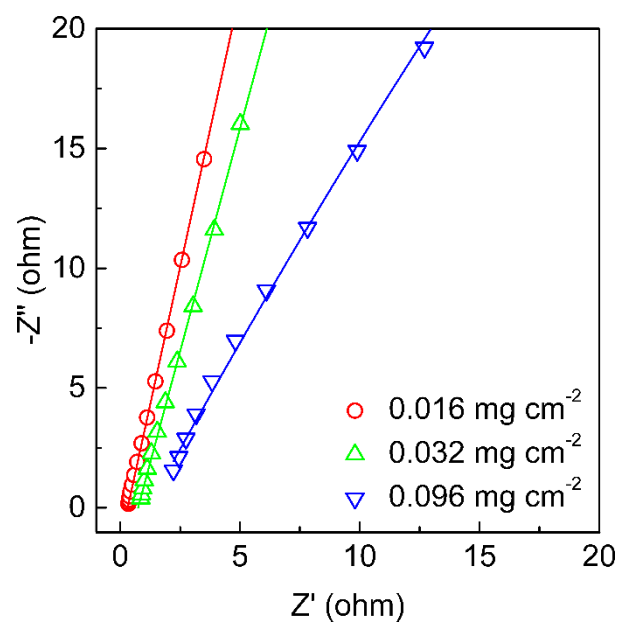
**Supplementary Figure 20.** Nyquist plots of $Ti_{0.87}O_2$/PP separators with different weight densities.
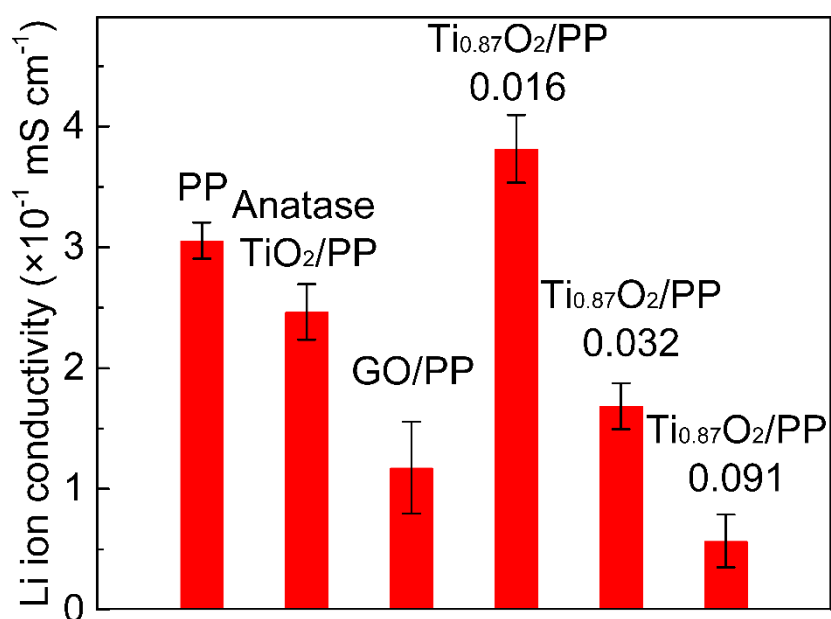
**Supplementary Figure 21.** Li ion conductivity of PP, anatase $TiO_2$/PP, GO/PP and $Ti_{0.87}O_2$/PP separators with different surface area mass loadings. Error bars were included, which represent the standard deviation of the data taken from five samples.
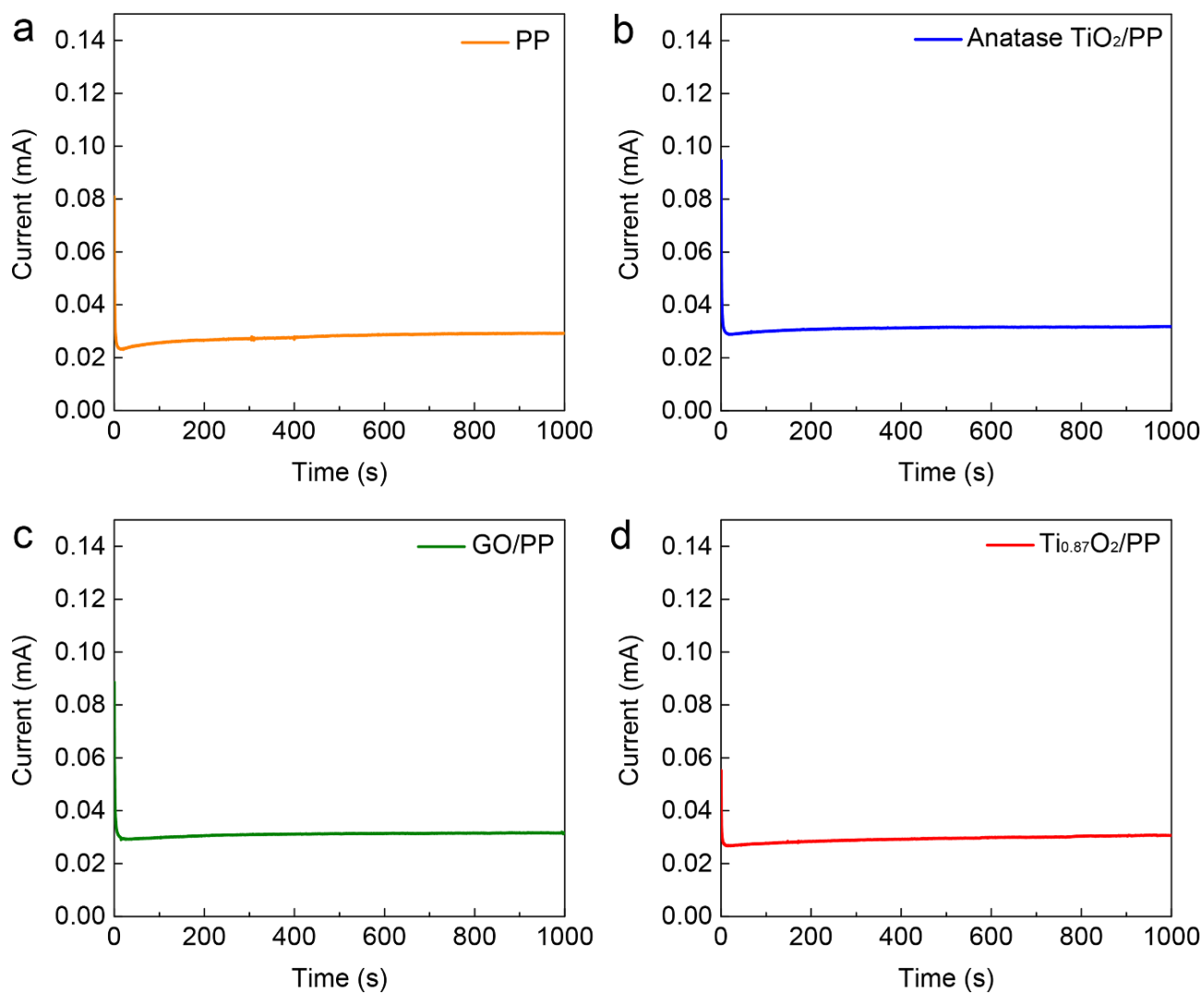
**Supplementary Figure 22.** Chronoamperometric measurements of PP, anatase $TiO_2$/PP, GO/PP and $Ti_{0.87}O_2$/PP separators.
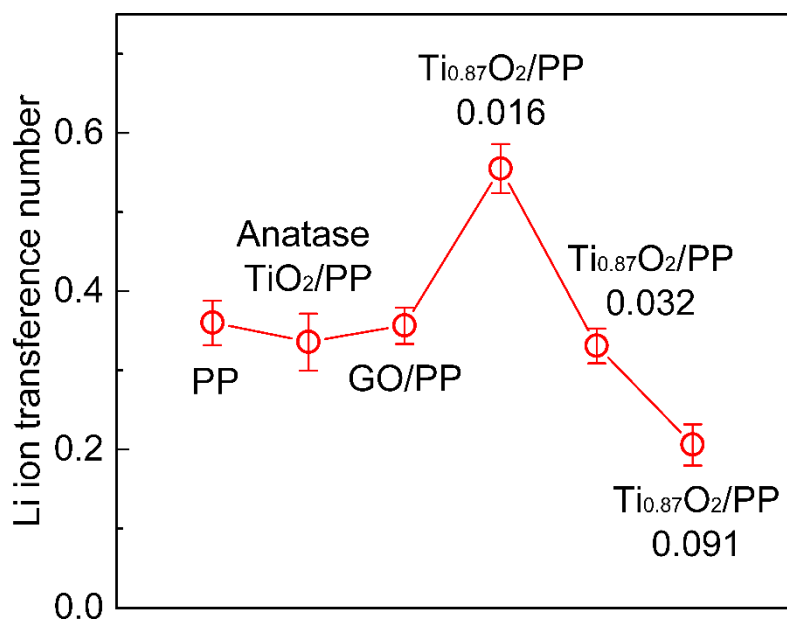
**Supplementary Figure 23.** Li ion transference number of PP, anatase $TiO_2$/PP, GO/PP and $Ti_{0.87}O_2$/PP separators with different surface area mass loadings. Error bars were included, which represent the standard deviation of the data taken from five samples.
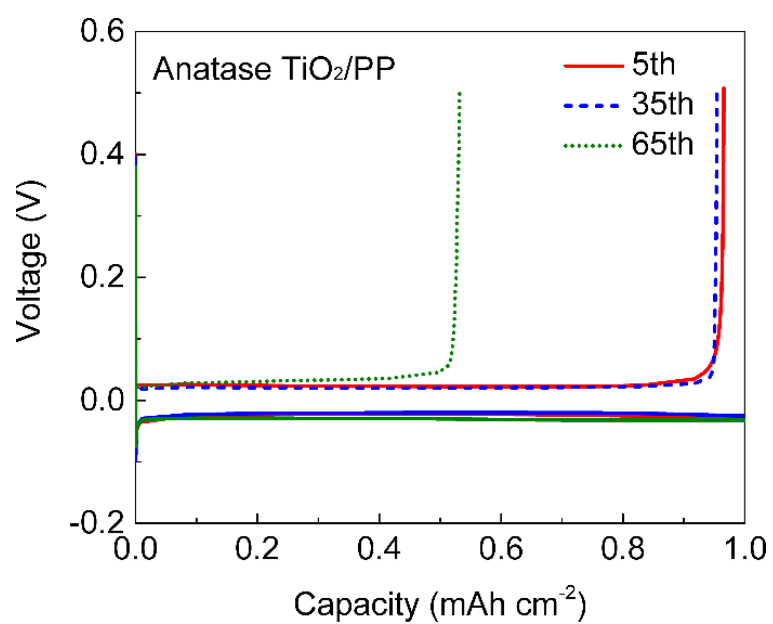
**Supplementary Figure 24.** Voltage profiles of Li plating/stripping processes in Li‖Cu cells with anatase TiO$_2$/PP separators with an areal capacity of 1 mAh cm$^{-2}$ at 1 mA cm$^{-2}$.
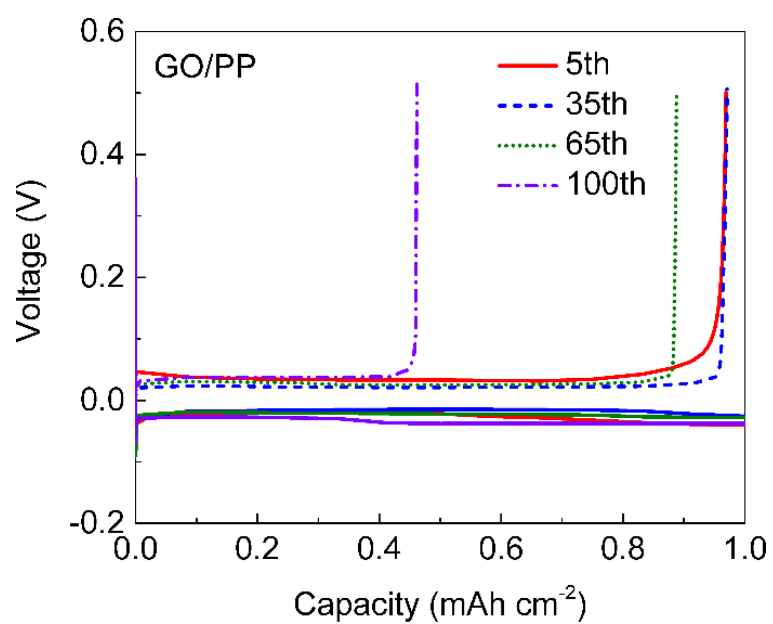
**Supplementary Figure 25.** Voltage profiles of Li plating/stripping processes in Li‖Cu cells with GO/PP separators with an areal capacity of 1 mAh cm$^{-2}$ at 1 mA cm$^{-2}$.
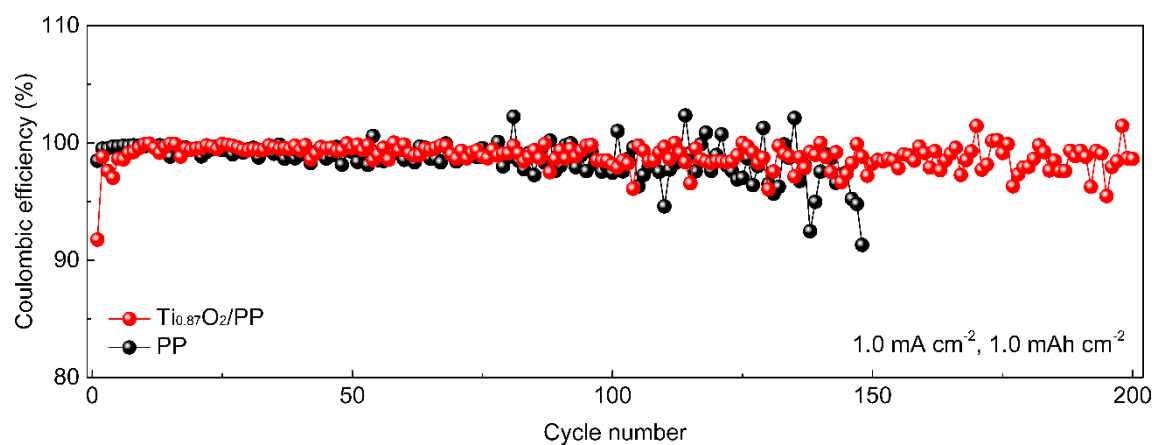
**Supplementary Figure 26.** Coulombic efficiencies of Na‖Cu cells with PP and $Ti_{0.87}O_2$/PP separators with an area capacity of 1 mAh cm$^{-2}$ at 1 mA cm$^{-2}$.
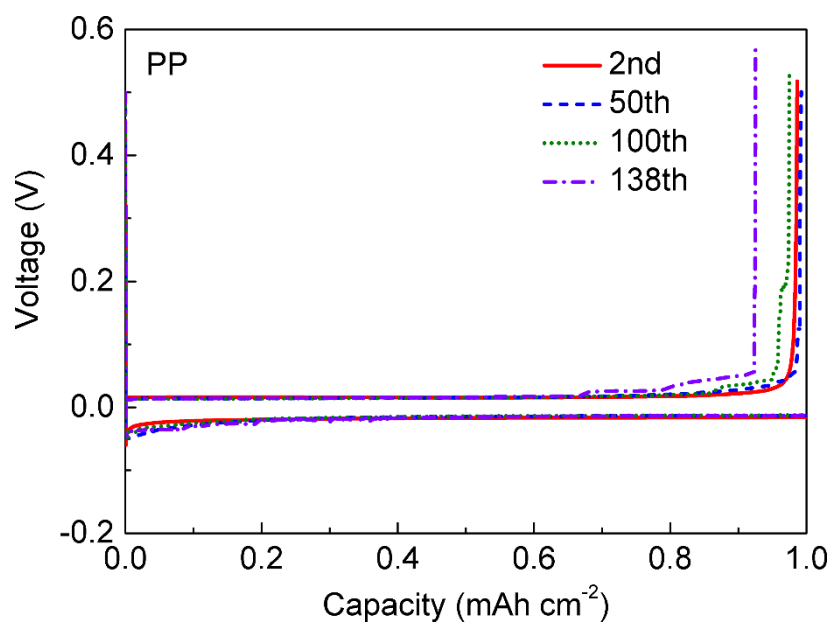
**Supplementary Figure 27.** Voltage profiles of Na plating/stripping processes in Na∥Cu cells with PP separators with an areal capacity of 1 mAh cm$^{-2}$ at 1 mA cm$^{-2}$.
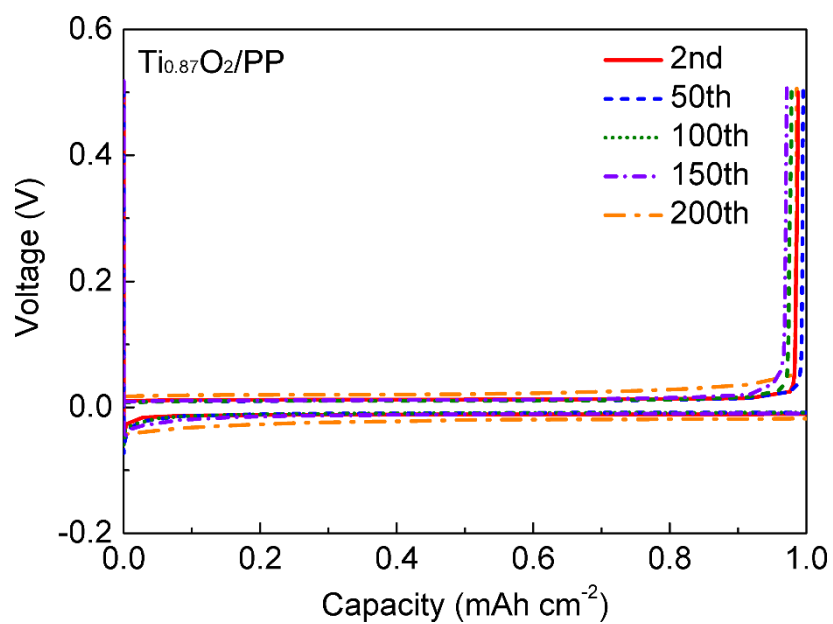
**Supplementary Figure 28.** Voltage profiles of Na plating/stripping processes in Na||Cu cells with Ti$_{0.87}$O$_2$/PP separators with an areal capacity of 1 mAh cm$^{-2}$ at 1 mA cm$^{-2}$.
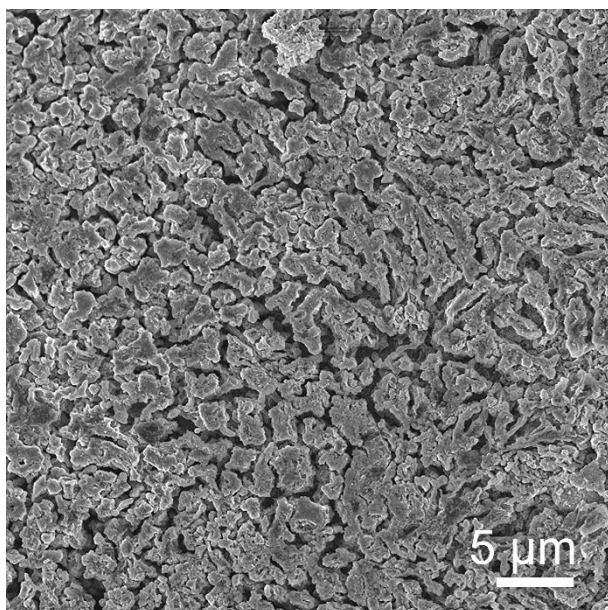
**Supplementary Figure 29.** SEM image of the Li metal anodes disassembled from the symmetrical cell with the PP separator at a current density of $2\,\mathrm{mA\,cm^{-2}}$ with a capacity of $1\,\mathrm{mAh\,cm^{-2}}$ for 20 cycles.
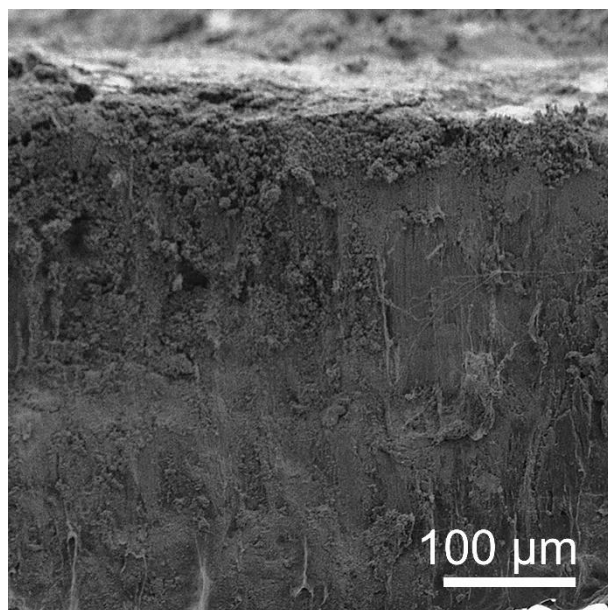
**Supplementary Figure 30.** Cross-section SEM image of the Li metal anodes disassembled from the symmetrical cell with the PP separator at a current density of $2\,\mathrm{mA\,cm^{-2}}$ with a capacity of 1 mAh $\mathrm{cm^{-2}}$ for 20 cycles.
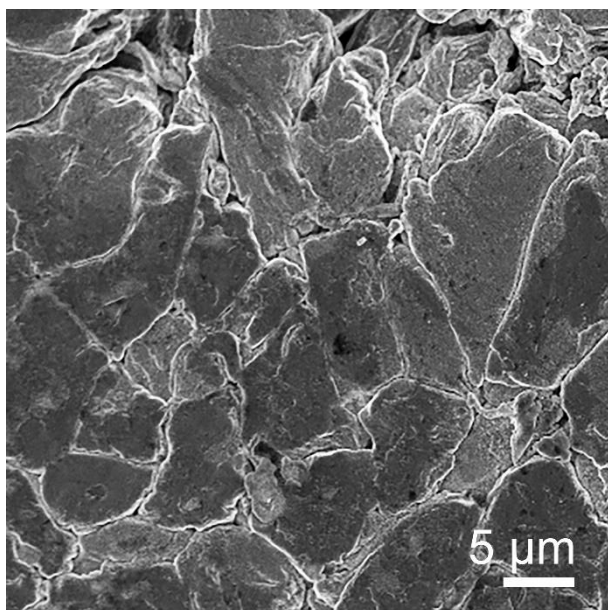
**Supplementary Figure 31.** SEM image of the Li metal anodes disassembled from the symmetrical cell with the $Ti_{0.87}O_2$/PP separator at a current density of 2 mA $cm^{-2}$ with a capacity of 1 mAh $cm^{-2}$ for 20 cycles.
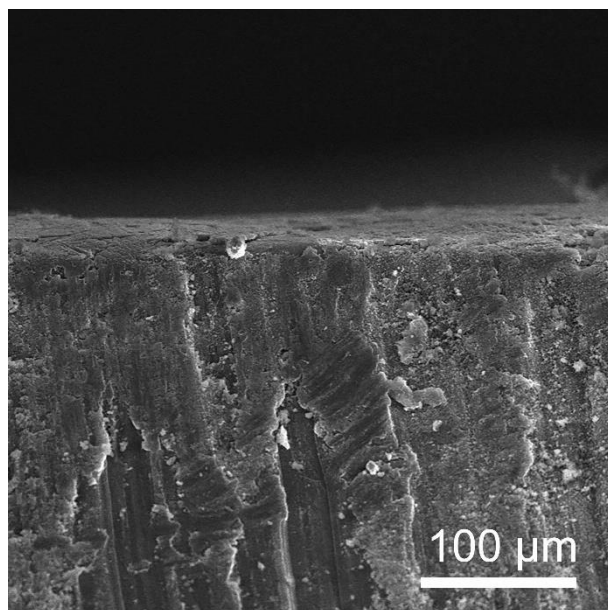
**Supplementary Figure 32.** Cross-section SEM image of the Li metal anodes disassembled from the symmetrical cell with the $Ti_{0.87}O_2$/PP separator at a current density of 2 mA cm$^{-2}$ with a capacity of 1 mAh cm$^{-2}$ for 20 cycles.
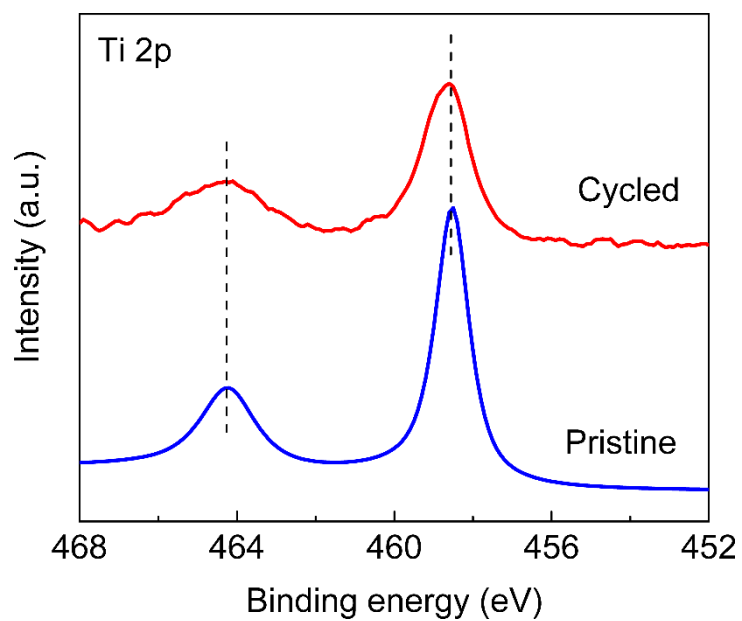
**Supplementary Figure 33.** High-resolution XPS spectrum of Ti 2p of pristine and cycled $Ti_{0.87}O_2$/PP separators disassembled from the symmetrical cell at a current density of $2\,\mathrm{mA\,cm^{-2}}$ with a capacity of $1\,\mathrm{mAh\,cm^{-2}}$ for 20 cycles.
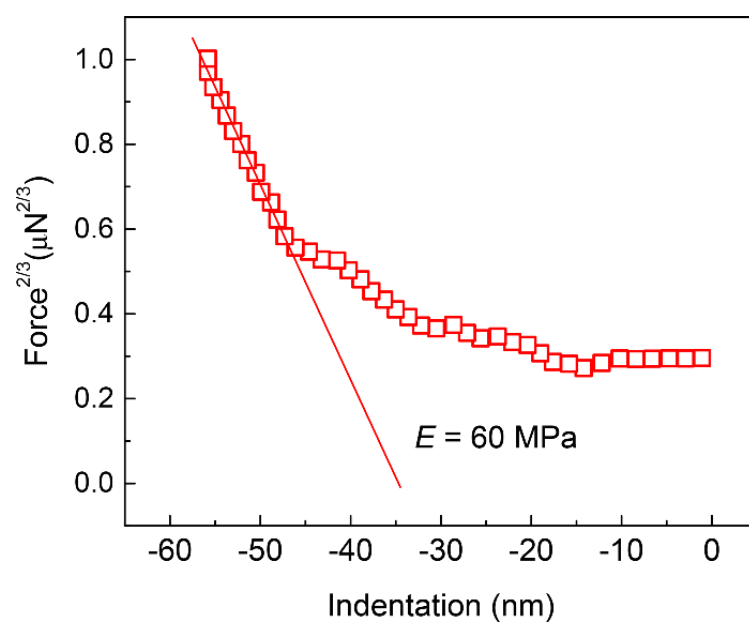
**Supplementary Figure 34.** A representative force-indentation curve of the $Ti_{0.87}O_2$/PP separator. The curve is fitted using the Hertzian model in the linear region.
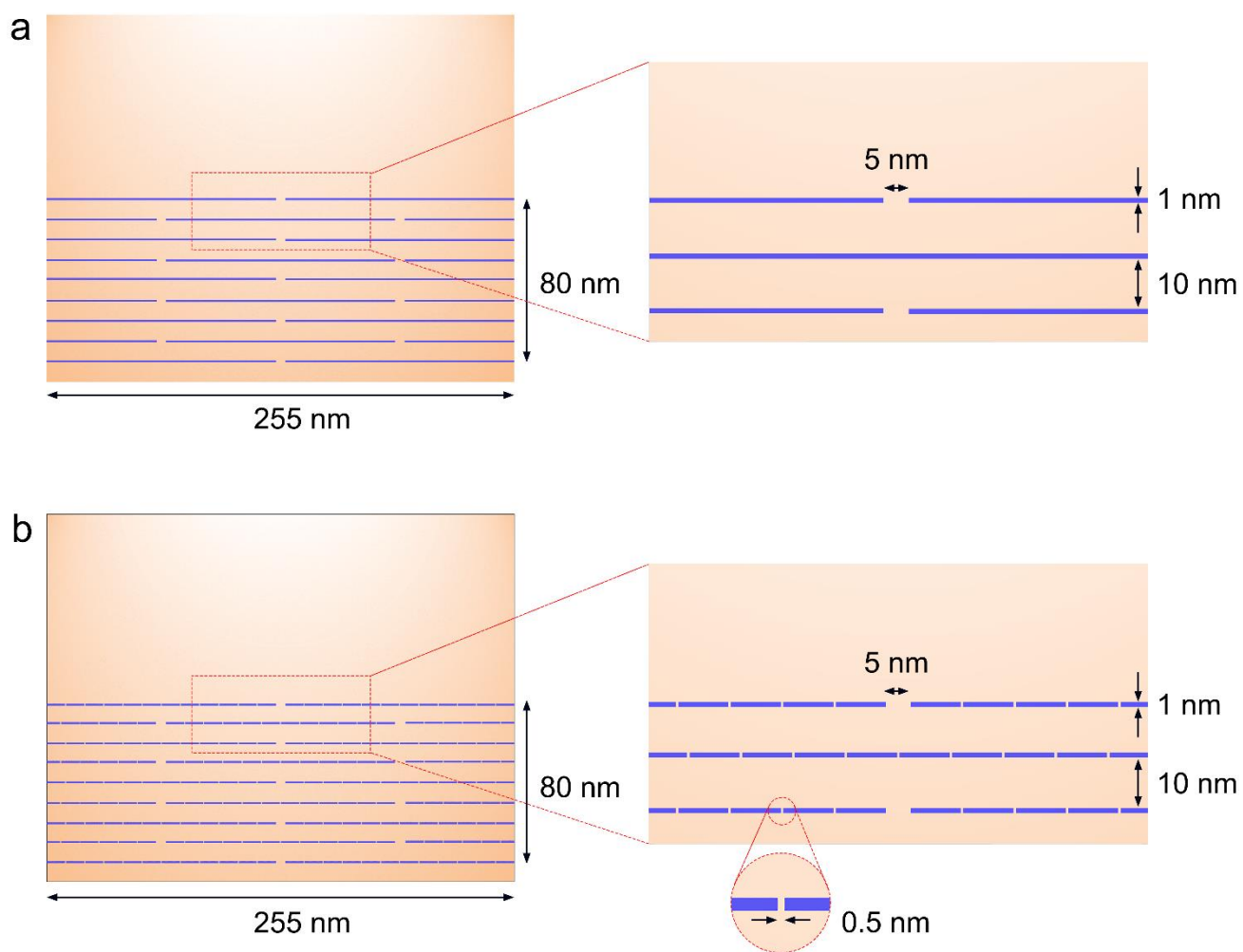
**Supplementary Figure 35.** The models of restacked thin layers for the (a) conventional nanosheets (without defects) and (b) defective nanosheets.
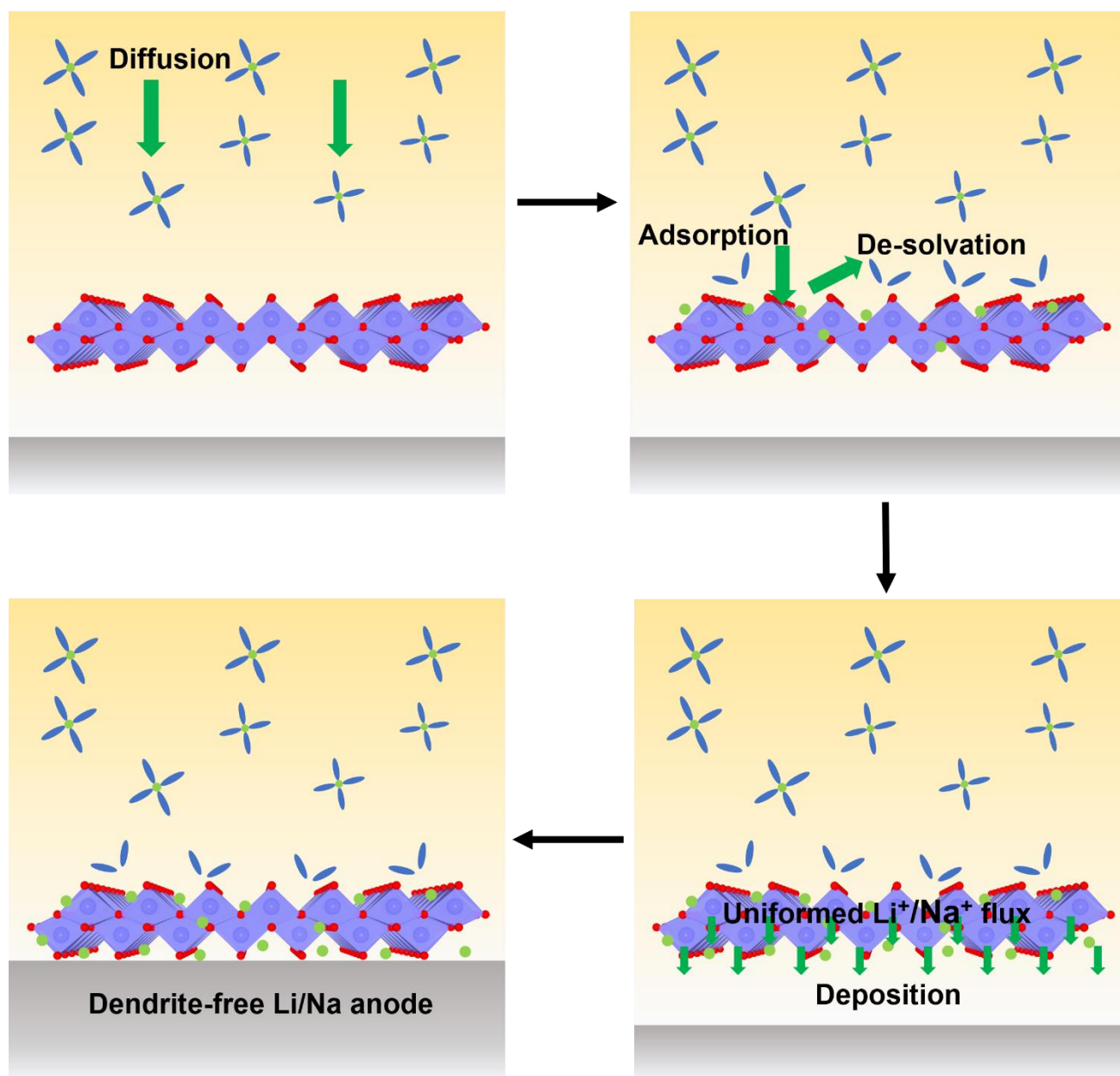
**Supplementary Figure 36.** Schematic illustration of mechanism of dendrite-free Li/Na anode by using anionic $Ti_{0.87}O_2$ nanosheets with atomic Ti vacancies.
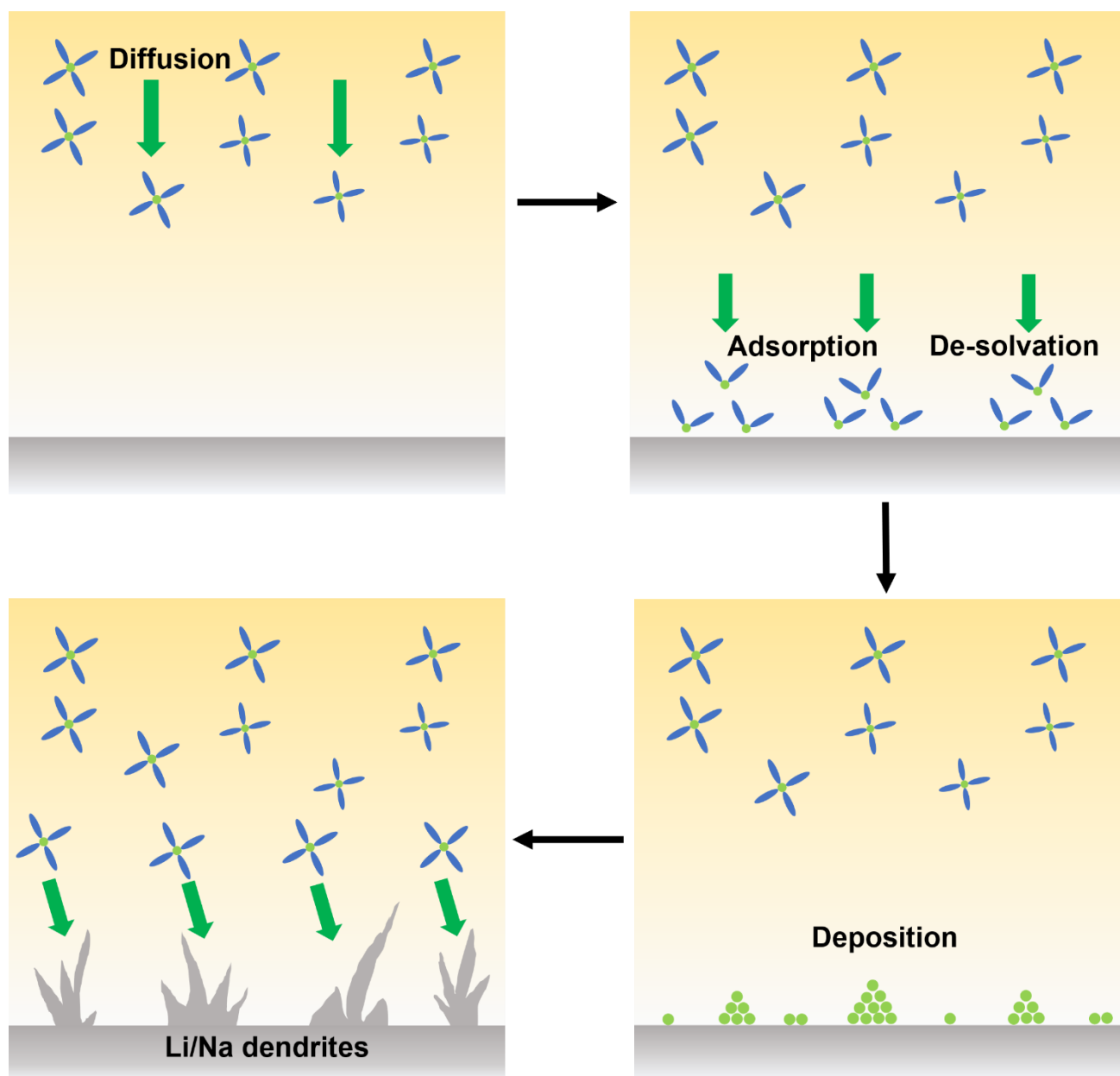
**Supplementary Figure 37.** Schematic illustration of Li/Na deposition over the bare anode.
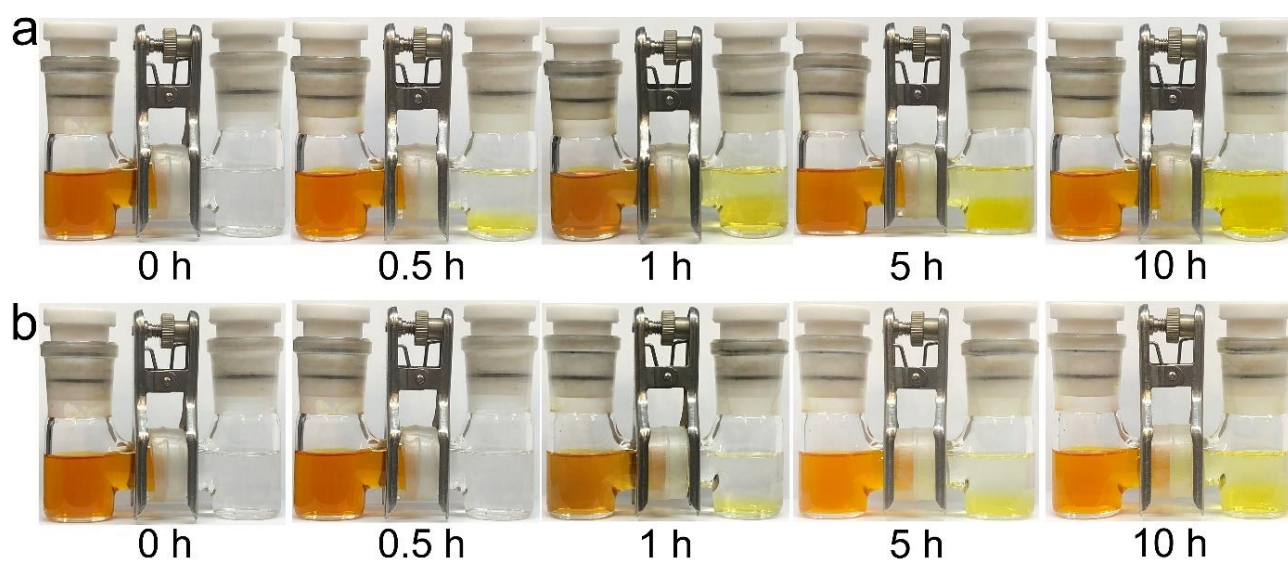
**Supplementary Figure 38.** Polysulfide permeation measurements in H-type cells with the (a) anatase TiO$_2$/PP and (b) GO/PP separators.
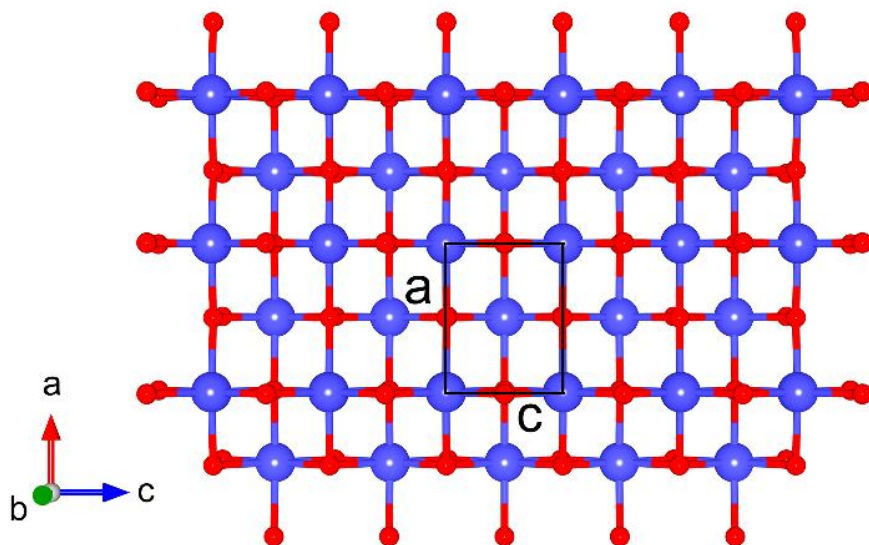
**Supplementary Figure 39.** Calculation of negative charge density of $Ti_{0.87}O_2^{0.52-}$ nanosheets. In-plane structure of $Ti_{0.87}O_2$ shows a rectangular unit cell with $a = 0.38$ nm and $c = 0.30$ nm. The 2D charge density ($\rho$) of $Ti_{0.87}O_2$ can be calculated based on the in-plane unit cell area, $\rho_{(Ti0.87O2)} = 2 \times 0.52 \times 1.60 \times 10^{-19} / (a \times c) = 1.46$ C m$^{-2}$.
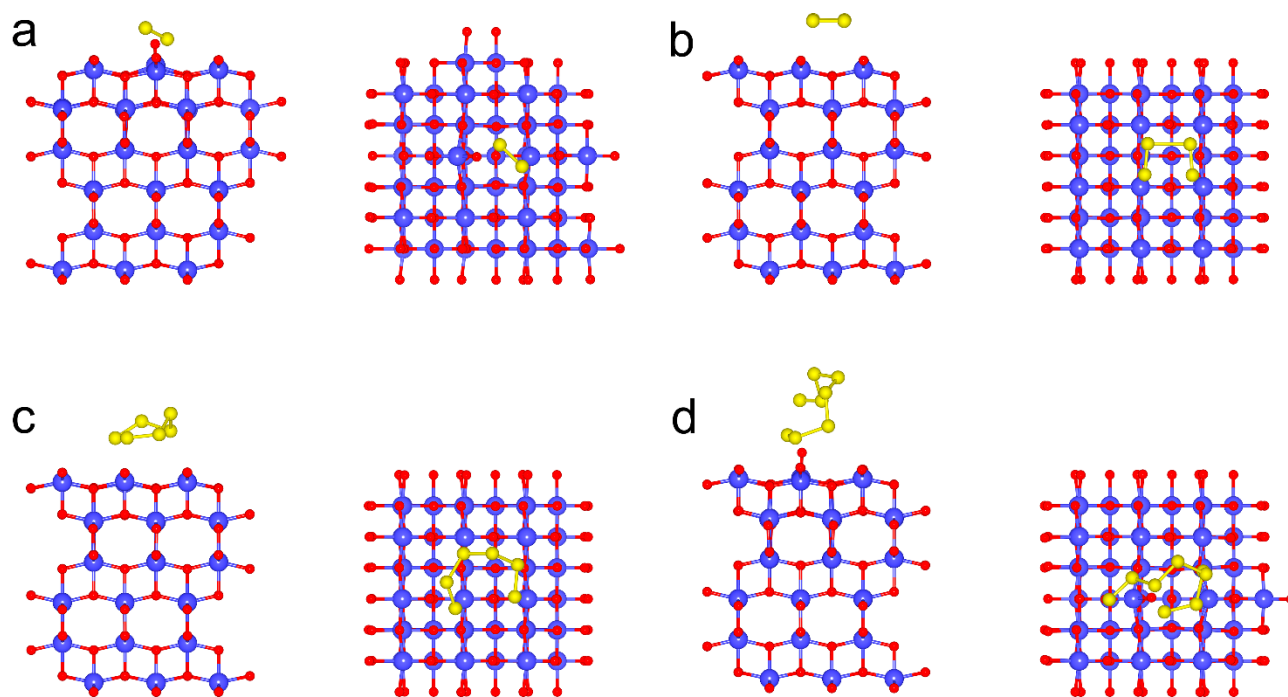
**Supplementary Figure 40.** Optimized conformations of (a) $S_2^{2-}$, (b) $S_4^{2-}$, (c) $S_6^{2-}$ and (d) $S_8^{2-}$ on anatase $TiO_2$.
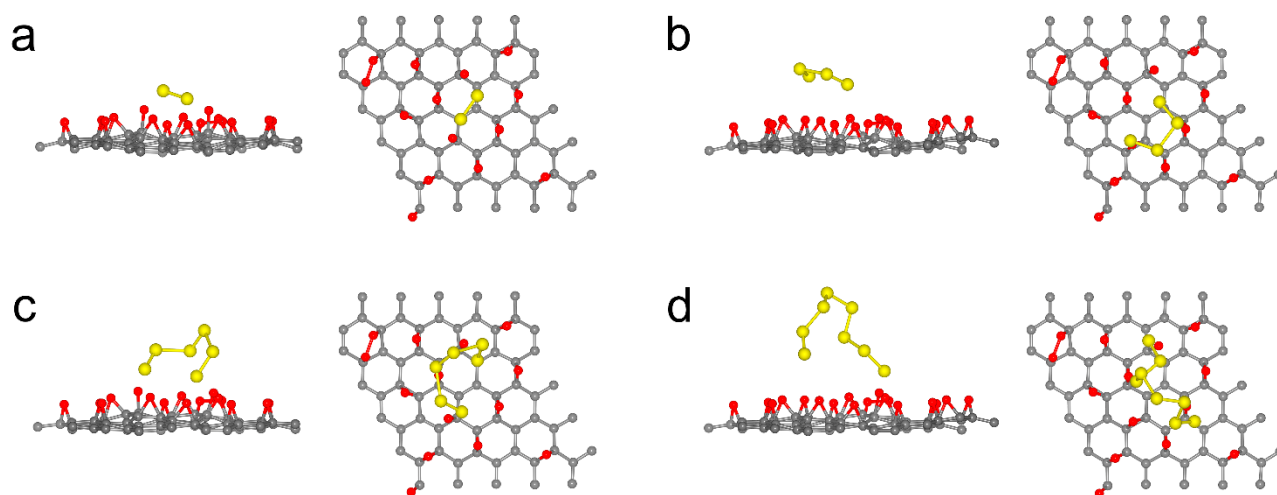
**Supplementary Figure 41.** Optimized conformations of (a) $S_2^{2-}$, (b) $S_4^{2-}$, (c) $S_6^{2-}$ and (d) $S_8^{2-}$ on GO sheet.
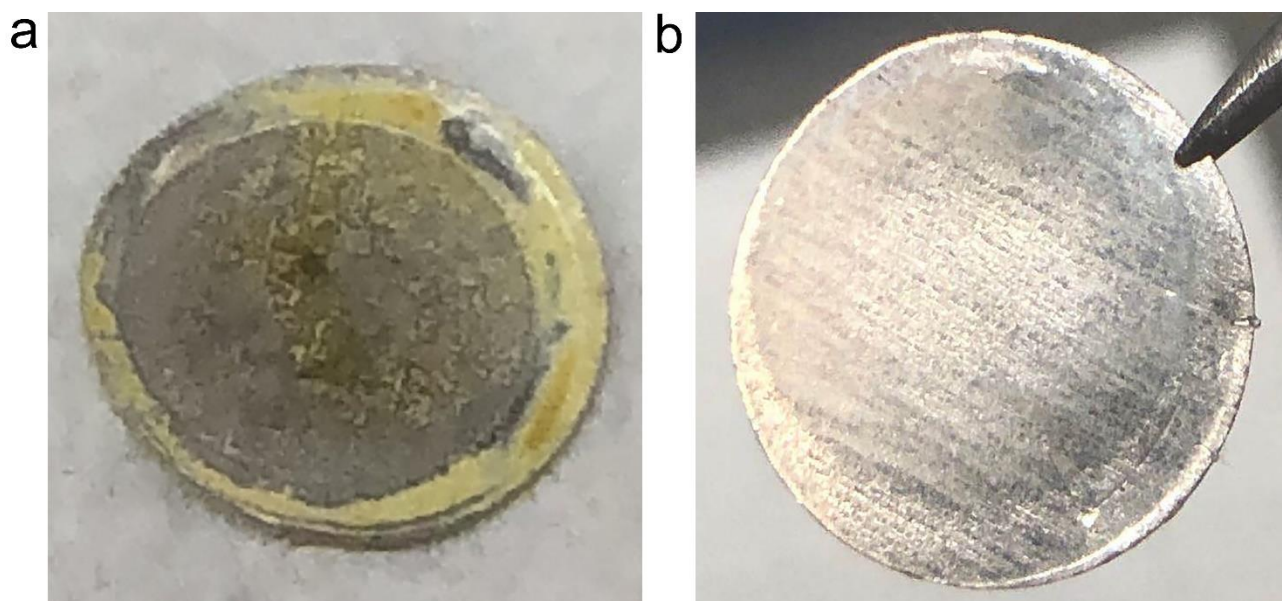
**Supplementary Figure 42.** Digital images of the Li metal anodes of the disassembled cells after10 cycles with the (a) PP and (b) $Ti_{0.87}O_2$/PP separators.
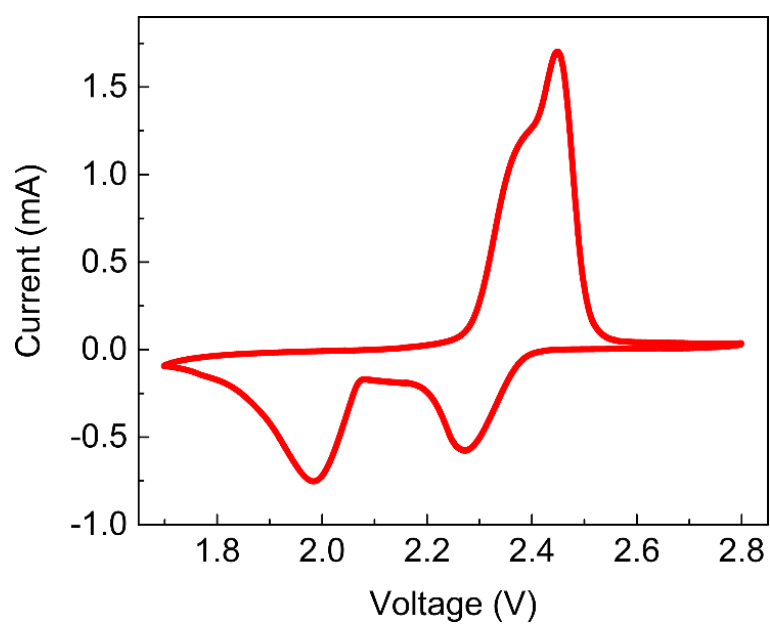
**Supplementary Figure 43.** CV curve of the Li–S cell with a $Ti_{0.87}O_2$/PP separator at 0.1 mV s$^{-1}$.
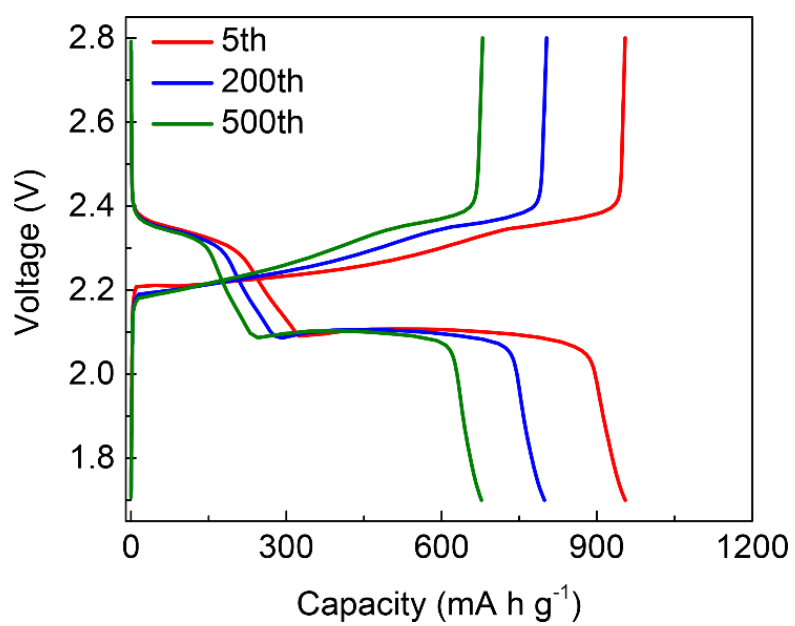
**Supplementary Figure 44.** Voltage profiles of the Li–S cell with a $Ti_{0.87}O_2$/PP separator at 0.2C.
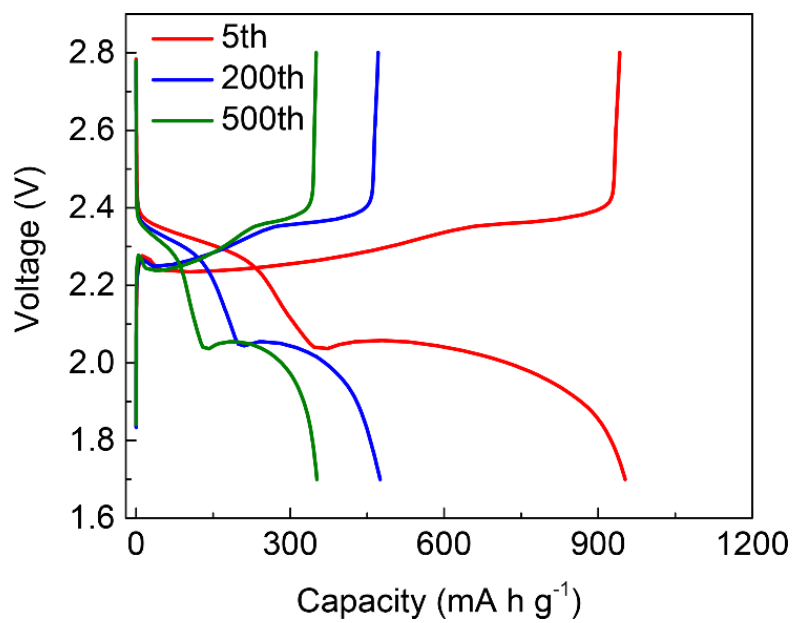
**Supplementary Figure 45.** Voltage profiles of the Li–S cell with a PP separator at 0.2C.
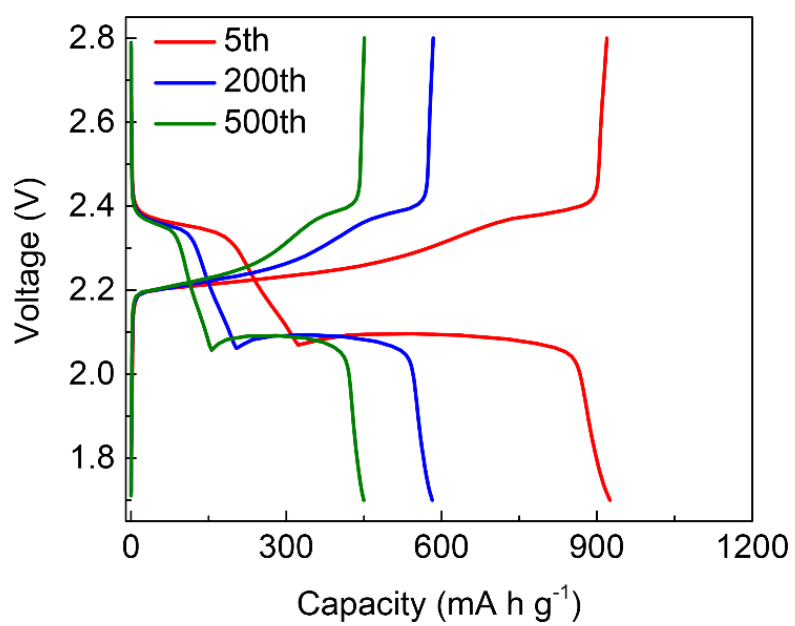
**Supplementary Figure 46.** Voltage profiles of the Li–S cell with an anatase $TiO_2$/PP separator at 0.2C.
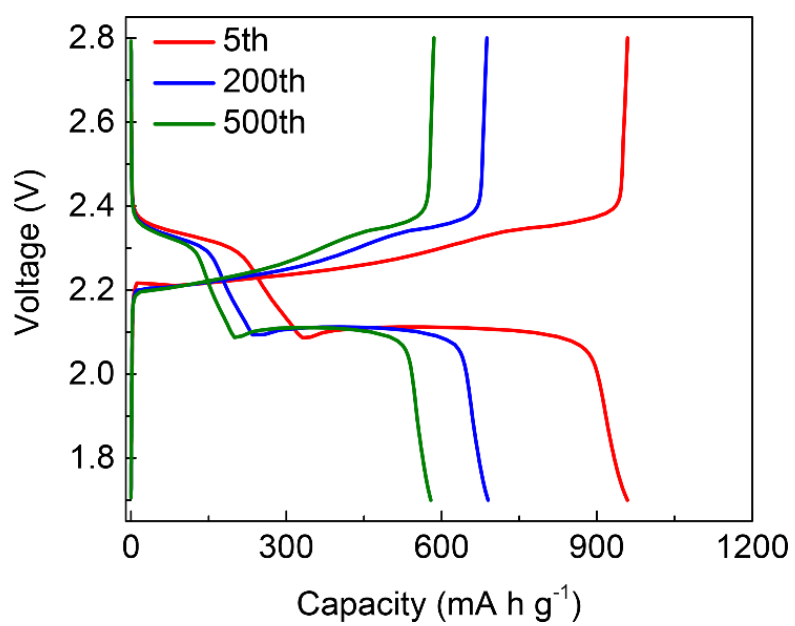
**Supplementary Figure 47.** Voltage profiles of the Li–S cell with a GO/PP separator at 0.2C.
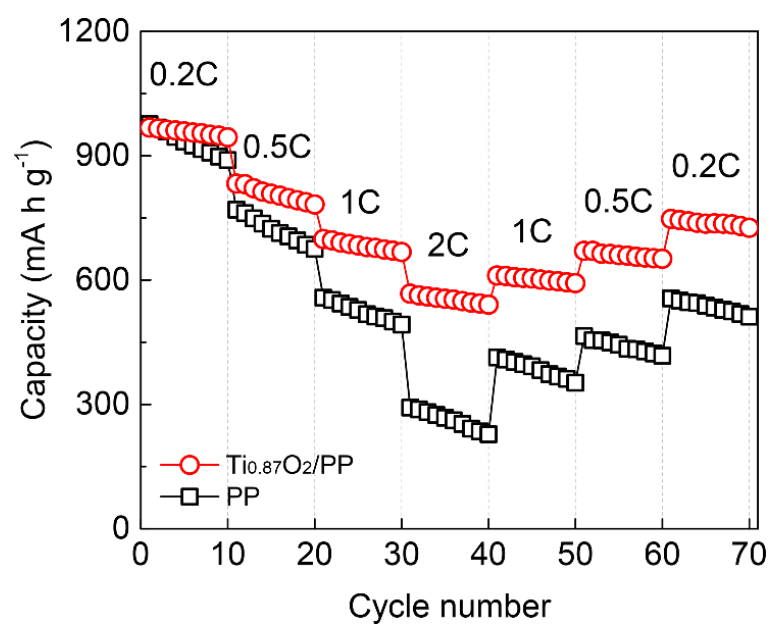
**Supplementary Figure 48.** The rate performance of Li–S cells with PP and $Ti_{0.87}O_2$/PP separators.
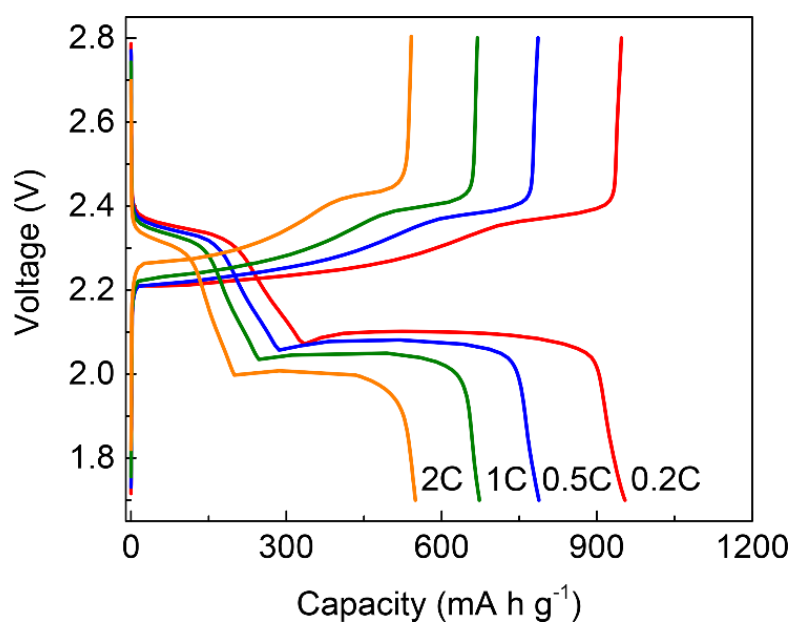
**Supplementary Figure 49.** Voltage profiles of the Li–S cell with a $Ti_{0.87}O_2$/PP separator at various C

rates.
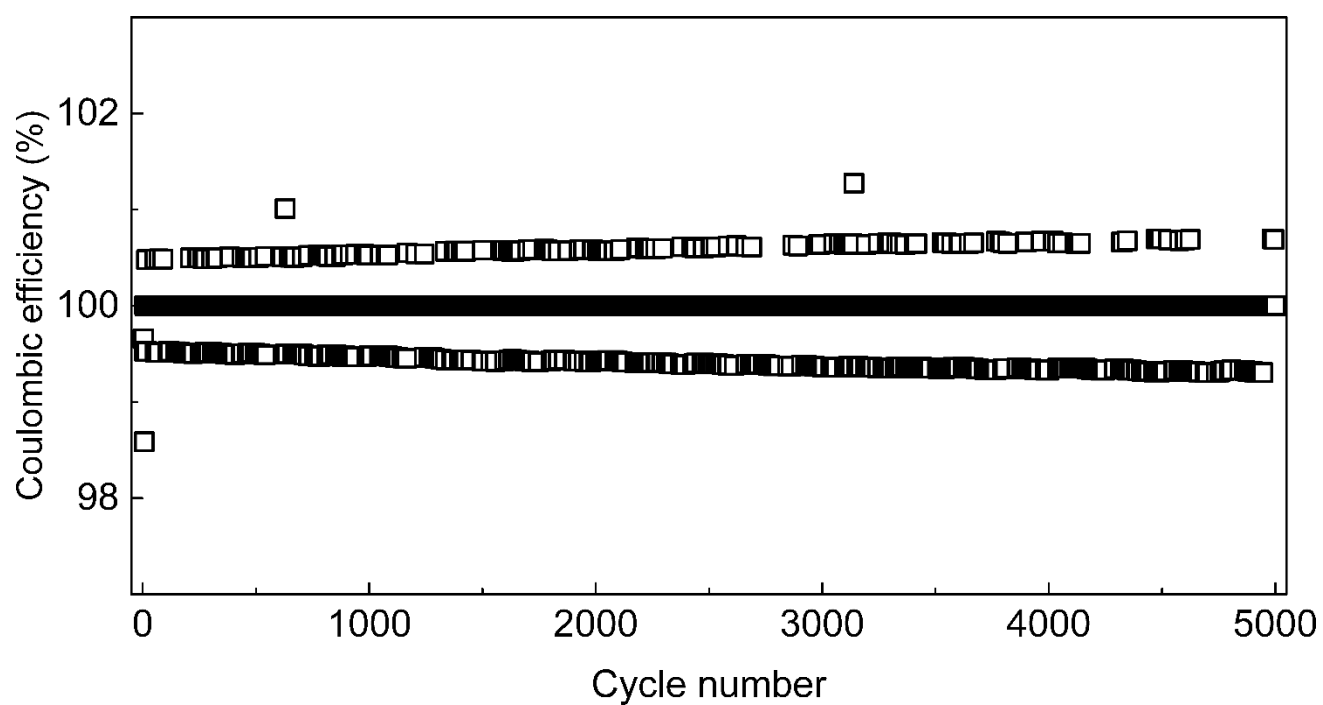
**Supplementary Figure 50.** Coulombic efficiency for a Li-S cell with a $Ti_{0.87}O_2$/PP separator during the long-term cycling at 1C for 5000 cycles.
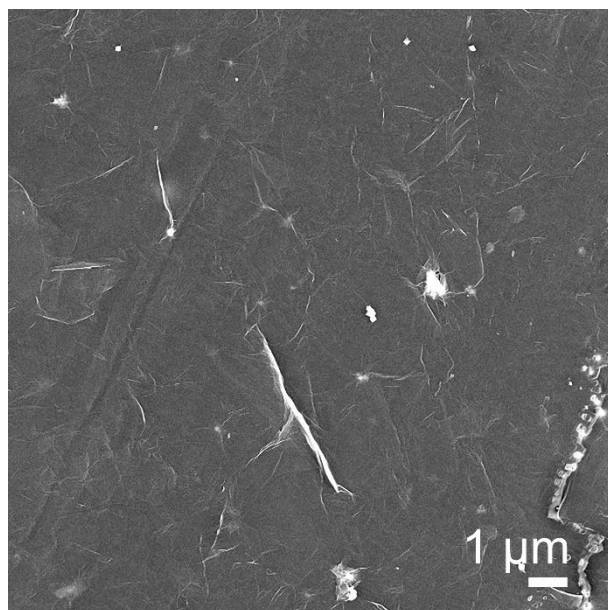
**Supplementary Figure 51.** SEM image of the cycled $Ti_{0.87}O_2$/PP separators from the disassembled cells in a fully discharged state after 500 cycles.
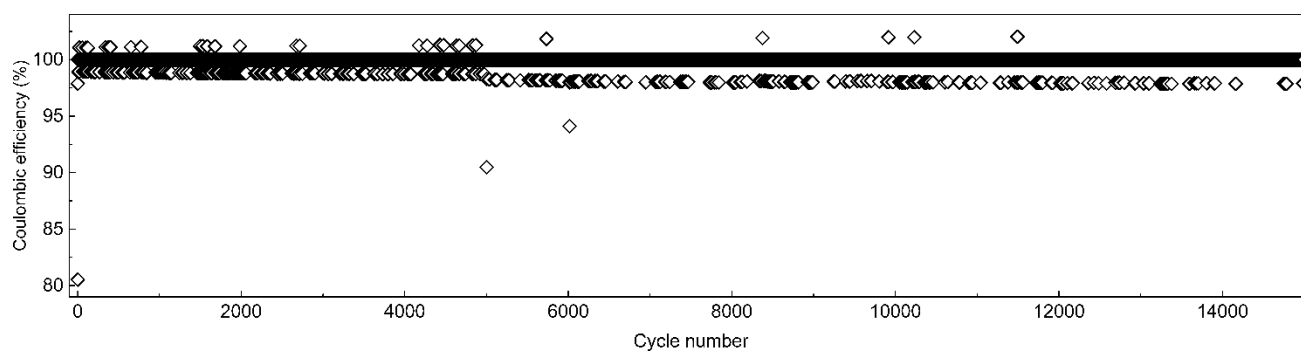
**Supplementary Figure 52.** Coulombic efficiency for a Li-S cell with a Ti$_{0.87}$O$_2$/PP separator at a sulfur mass loading of 3.5 mg cm$^{-2}$ during the long-term cycling.
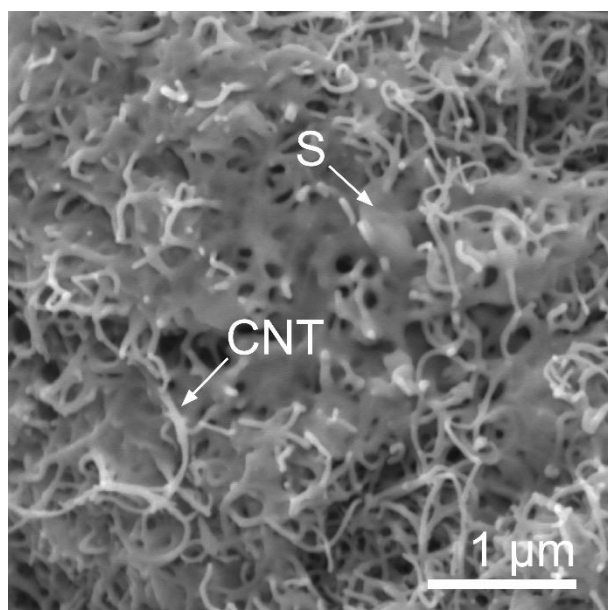
**Supplementary Figure 53.** SEM image of the CNT/S cathodes.
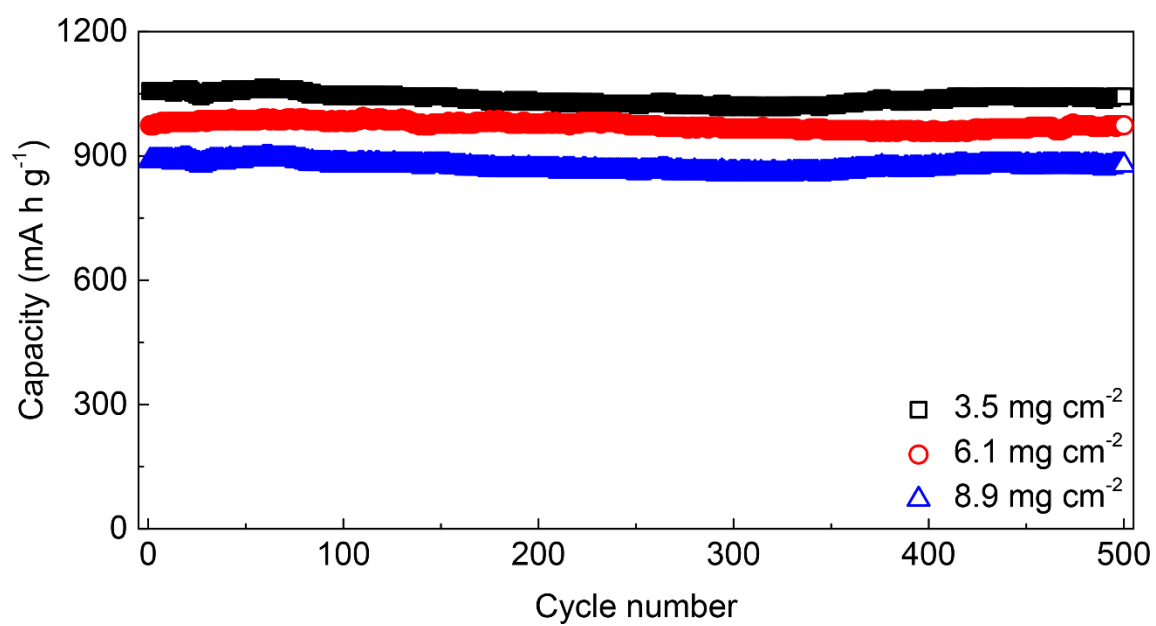
**Supplementary Figure 54.** Cycling performance of the Li-S cells at 0.2C using the CNT/S cathodes and the $Ti_{0.87}O_2$/PP separators.
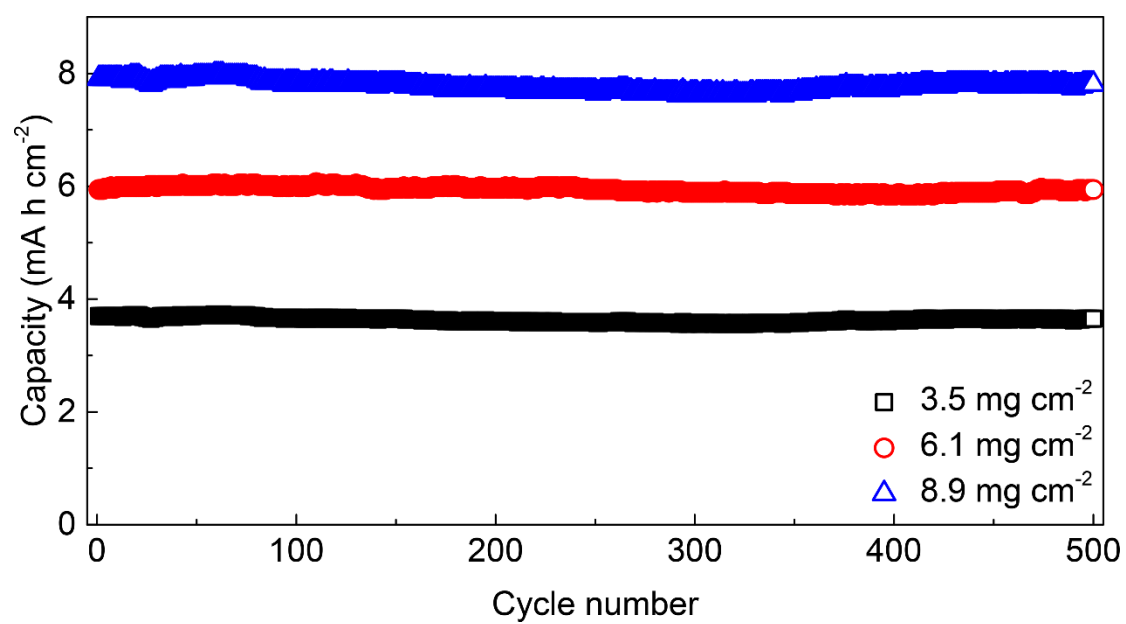
**Supplementary Figure 55.** Areal capacities of the Li-S cells using the CNT/S cathodes and the $Ti_{0.87}O_2$/PP separators.
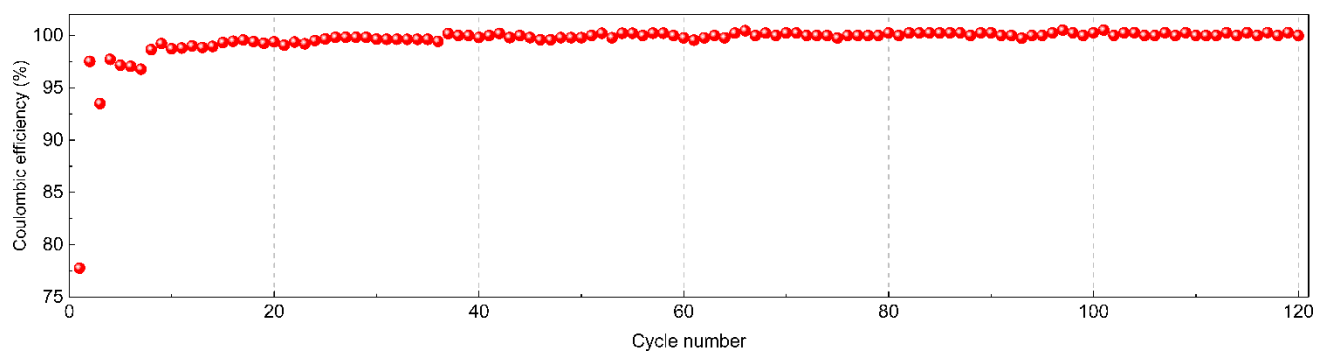
**Supplementary Figure 56.** Coulombic efficiency for a flexible Li-S pouch cell with a $Ti_{0.87}O_2$/PP

separator under different bending angles during the cycling test.
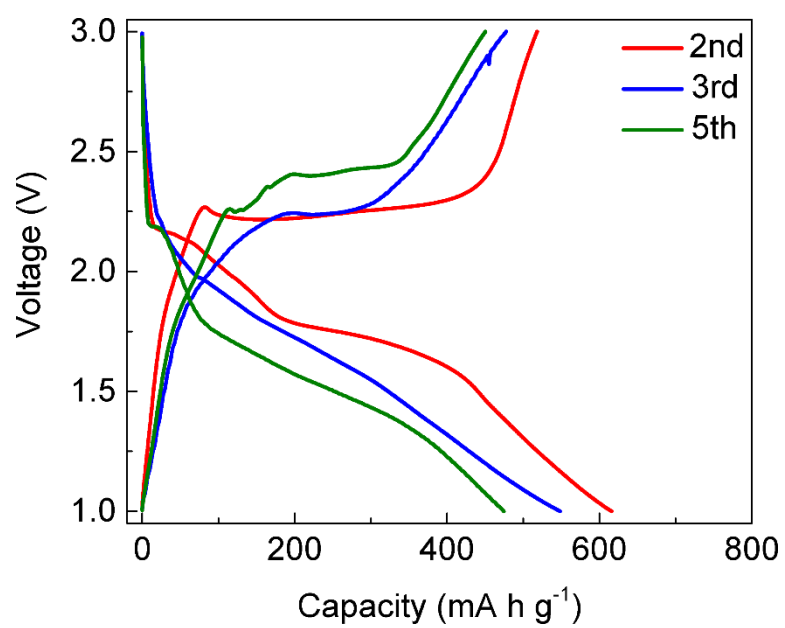
**Supplementary Figure 57.** Voltage profiles of the Li–Se cell with a PP separator at 0.2C.
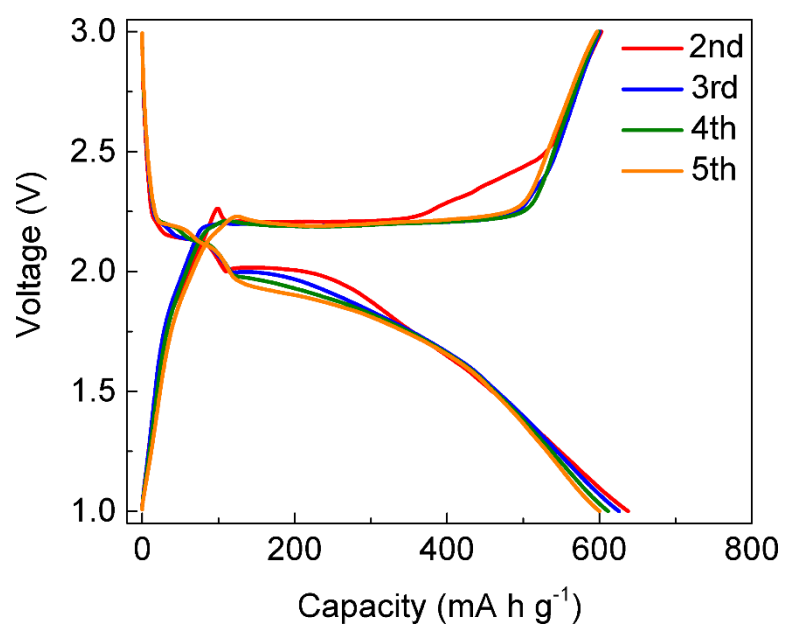
**Supplementary Figure 58.** Voltage profiles of the Li–Se cell with a $Ti_{0.87}O_2$/PP separator at 0.2C.
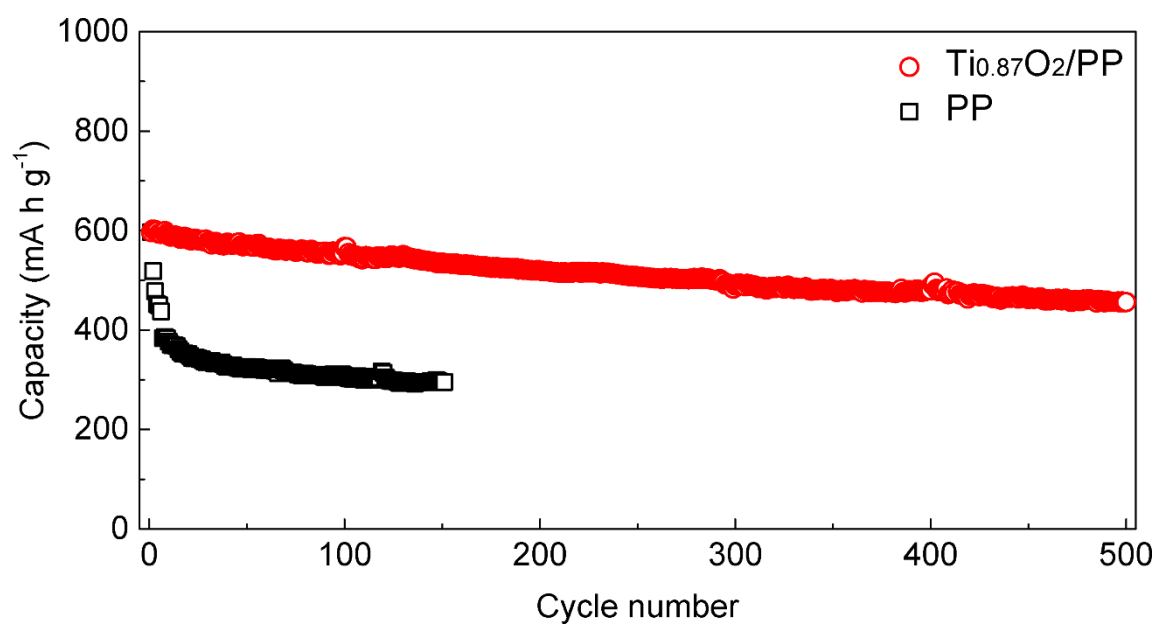
**Supplementary Figure 59.** Cycling performance of the Li-Se cells at 0.2C with PP and $Ti_{0.87}O_2$/PP
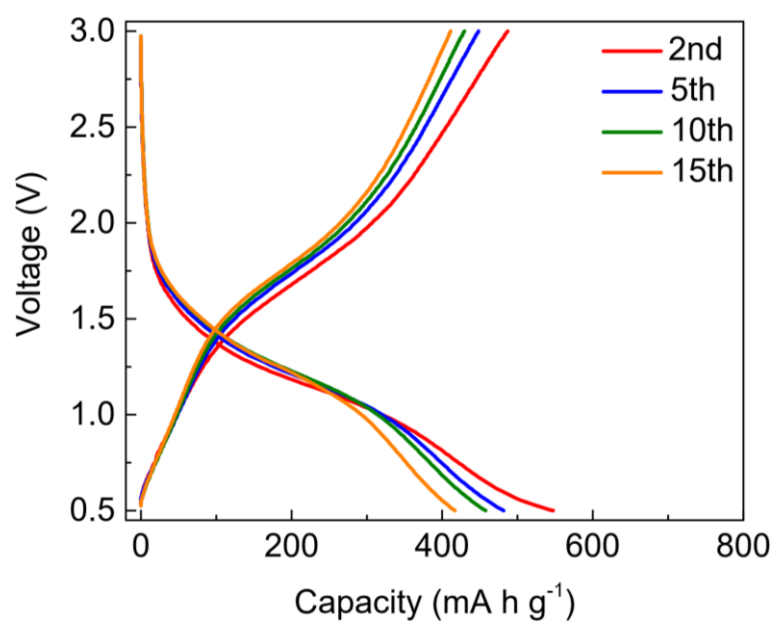
separators.

**Supplementary Figure 60.** Voltage profiles of the Na–Se cell with a PP separator at 0.2C.
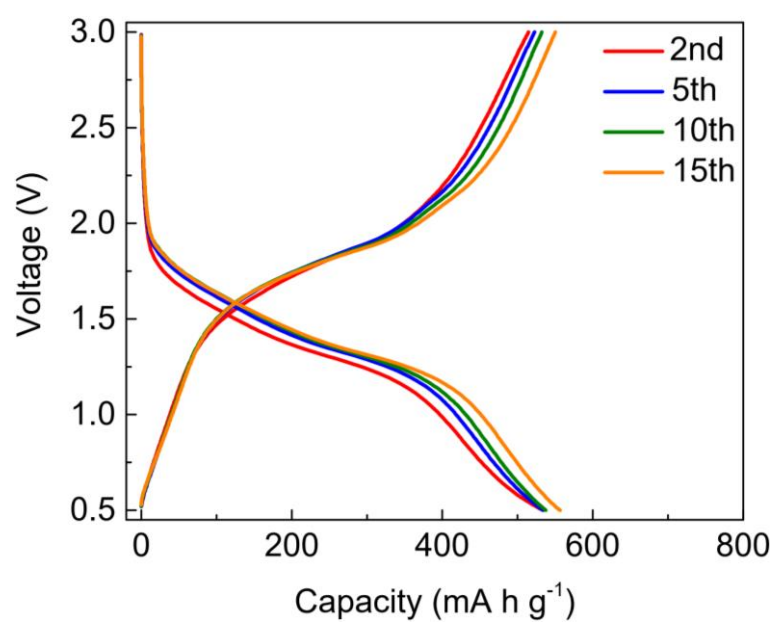
**Supplementary Figure 61.** Voltage profiles of the Na–Se cell with a $Ti_{0.87}O_2$/PP separator at 0.2C.
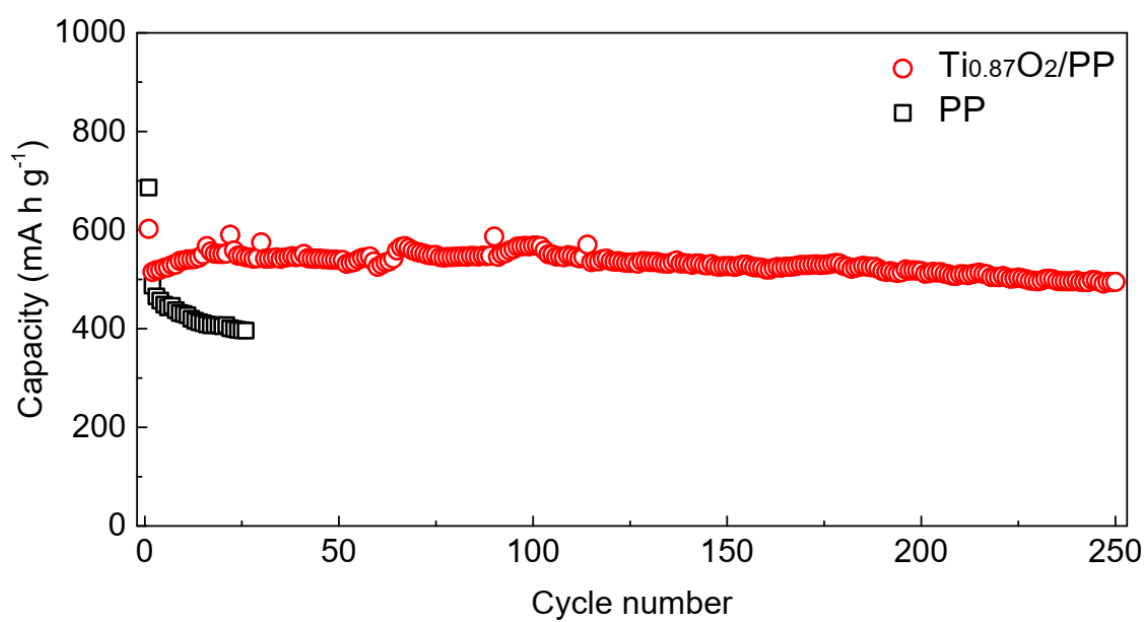
**Supplementary Figure 62.** Cycling performance of the Na-Se cells at 0.2C with PP and $Ti_{0.87}O_2$/PP separators.

**Supplementary Movie 1.** Molecular dynamic simulation of the diffusion of polysulfide anions and Li ions through the anionic $Ti_{0.87}O_2$ monolayer with one Ti vacancy.

**Supplementary Table 1.** Electrochemical properties of various functional separators in Li-S cells.

| Functional separators | | | | | | Battery performance | | |
|---|---|---|---|---|---|---|---|---|
| Materials | Surface area mass loading (mg cm$^{-2}$) | Thickness (μm) | Cathode composite active material | S wt.% (mg cm$^{-2}$) | Voltage range (V) | Electrolyte | Cycling performance (cycles, C-rates (1C= 1675 mA g$^{-1}$), capacity decay rate) | Ref |
| GO | 0.12 | 5 | Carbon black/S | 1.0-1.5 | 1.5-3.0 | 1 M LiTFSI in DOL/DME (v/v = 1:1) | 100, 0.1C, 0.23% | 1 |
| Nafion/GO | 0.128 | 0.030 | Garphene/ CNT/S | 1.2 | 1.5-3.0 | 1 M LiTFSI in DOL/DME (v/v = 1:1) | 200, 0.1C, 0.18% | 2 |
| Commercial graphene | 1.3 | 30 | Carbon black/S | 1.5-2.1 | 1.5-2.8 | 1 M LiTFSI in DOL/DME (v/v = 1:1) with 1.0 wt% LiNO$_3$ | 500, 0.9C, 0.064% | 3 |
| CVD-derived porous graphene | 0.54 | 10 | CNT/S | 1.8–2.0 | 1.8-2.8 | 1 M LiTFSI in DOL/DME (v/v = 1:1) with 1.0 wt% LiNO$_3$ | 150, 0.5C, 0.16% | 4 |
| Commercial graphene@ porous carbon (G@PC) | 0.075 | 0.9 | Carbon black/S | 3.5 | 1.6-2.8 | 1 M LiTFSI in DOL/DME (v/v = 1:1) with 2.0 wt% LiNO$_3$ | 100, 0.2C, 0.08% | 5 |

| | | | | | | | | |
|---|---|---|---|---|---|---|---|---|
| Co/N-carbon sheets/reduced graphene oxide | 0.2 | 41.3 | CNT/S | 1.0 | 1.7-2.8 | 1 M LiTFSI in DOL/DME (v/v = 1:1) with 1.0 wt% LiNO$_3$ | 500, 0.2C, 0.07% | 6 |
| Cellular CVD-derived graphene framework | 0.3 | 30 | CNT/S | 1.2 | 1.7-2.8 | 1 M LiTFSI in DOL/DME (v/v = 1:1) | 300, 0.8375C, 0.085% | 7 |
| B-rGO | 0.2-0.3 | 25 | CNT/S | 1.45-1.56 | 1.8-2.8 | 1 M LiTFSI in DOL/DME (v/v = 1:1) with 0.2 M LiNO$_3$ | 300, 0.1C, 0.1532% | 8 |
| rGO@sodium lignosulfonate (rGO@SL) | 0.2 | ~20 | Carbon black/S | 1.5 | 1.7-2.7 | 1 M LiTFSI in DOL/DME (v/v = 1:1) with 1.0 wt% LiNO$_3$ | 1000, 2C, 0.026% | 9 |
| CNTs/N-doped carbon quantum dot (CNT/NCQD) | 0.15 | 25~30 | Carbon black/S | 1.3-1.5 | 1.8-2.7 | 1 M LiTFSI in DOL/DME (v/v = 1:1) with 2.0 wt% LiNO$_3$ | 1000, 0.5C, 0.05% | 10 |
| CNF-Gum Arabic | 0.25 | 19 | CNF/S | 1.1 | 1.7-2.8 | 1 M LiTFSI in DOL/DME (v/v = 1:1) | 250, 1C, 0.024% | 11 |

| | | | | | | | | |
|---|---|---|---|---|---|---|---|---|
| | | | | | | with 2.0 wt% LiNO$_3$ | | |
| Mg$_2$Al-LDH | 0.018 | 0.02-0.03 | Carbon black/S | 1.2-1.4 | 1.7-2.8 | 1 M LiTFSI in DOL/DME (v/v = 1:1) with 1.0 wt% LiNO$_3$ | 200, 0.5C, 0.18% | 12 |
| NiFe-LDH/CVD-derived N-doped graphene | 0.3 | 1.5 | Carbon/S | 1.2 | 1.7-2.8 | 1 M LiTFSI in 2.5 M Li$_2$S$_8$/tetraglyme | 1000, 2C, 0.06% | 13 |
| MoS$_2$ | - | 0.350 | Carbon black/S | - | 1.5-3.0 | 1 M LiTFSI in DOL/DME (v/v = 1:1) with 1.0 wt% LiNO$_3$ | 600, 0.5C, 0.083% | 14 |
| MoS$_2$-PDDA/PAA | 0.1 | 3 | Carbon black/S | 1.2-4.0 | 1.7-2.6 | 1 M LiTFSI in DOL/DME (v/v = 1:1) with 1.0 wt% LiNO$_3$ | 2000, 1C, 0.029% | 15 |
| Co$_9$S$_8$ | 0.16 | - | Carbon black/S | 2.0 | 1.8-2.8 | 1.85 M LiCF$_3$SO$_3$ in DOL/DME (v/v = 1:1) with 0.1 M LiNO$_3$ | 1000, 1C, 0.039% | 16 |

| Material | | | | | | Electrolyte | | Ref. |
|---|---|---|---|---|---|---|---|---|
| $Sb_2Se_{3-x}$/rGO | 0.5 | 32 | Carbon black/S | 1.8 | 1.7-2.8 | 1 M LiTFSI in DOL/DME (v/v = 1:1) with 1.0 wt% $LiNO_3$ | 500, 1C, 0.027% | 17 |
| MoP/rGO | 0.35-0.45 | 10 | Carbon/S | 3.6-4.0 | 1.8-2.8 | 0.6 M LiTFSI in DOL/DME (v/v = 1:1) with 0.4 M $LiNO_3$ | 120, 0.1C, 0.045% | 18 |
| $Ti_3C_2$ MXene | 0.1 | 0.522 | Carbon black/S | 1.2 | 1.7-2.8 | 1 M LiTFSI in DOL/DME (v/v = 1:1) with 0.1 M $LiNO_3$ | 500, 0.5C 0.062% | 19 |
| Black Phosphorus | 0.4 | ~0.35 | Carbon black/S | 1.5–2 | 1.7-2.6 | 1 M LiTFSI in DOL/DME (v/v = 1:1) with 1.0 wt% $LiNO_3$ | 100, 0.2C, 0.14% | 20 |
| Super P/Red phosphorus | 0.3 | 8 | Carbon black/S | 2 | 1.5-3.0 | 1 M LiTFSI in DOL/DME (v/v = 1:1) with 0.1 M $LiNO_3$ | 500, 1C, 0.036% | 21 |
| BN-carbon | - | 6~7 | Carbon black/S | 2.1 | 1.5-3.0 | 1 M $LiPF_6$ in EC/DEC (v/v = 1:1) | 250, 0.5C, 0.0936% | 22 |

| | | | | | | | | |
|---|---|---|---|---|---|---|---|---|
| BaTiO$_3$ | 2.4 | 18-23 | Carbon black/S | 3.2 | 1.8-2.6 | 1 M LiTFSI in DOL/DME (v/v = 1:1) with 0.3 M LiNO$_3$ | 50, 0.1C, 0.34% | 23 |
| H$_x$MnO$_{2+x}$/liquid phase-exfoliated graphene/CNTs | 0.2 | 3 | CNT/S | 1.8 | 1.7-2.8 | 1 M LiTFSI in DOL/DME (v/v = 1:1) with 1.0 wt% LiNO$_3$ | 1000, 1C, 0.04% | 24 |
| TiO$_2$/commercial graphene | 0.15 | 3 | CNT/S | 1.2 | 1.8-2.8 | 1 M LiTFSI in DOL/DME (v/v = 1:1) with 1.0 wt% LiNO$_3$ | 300, 0.5C, 0.01% | 25 |
| Li$_4$Ti$_5$O$_{12}$/chemically exfoliated graphene | 0.346 | 35 | Carbon black/S | 1.0-1.2 | 1.7-2.8 | 1 M LiTFSI in DOL/DME (v/v = 1:1) with 1.0 wt% LiNO$_3$ | 500, 1C, 0.028% | 26 |
| Ni$_3$(HITP)$_2$ | 0.066 | 0.34 | CNT/S | 8 | 1.7-2.8 | 1 M LiTFSI in DOL/DME (v/v = 1:1) with 2.0 wt% LiNO$_3$ | 500, 1C, 0.066% | 27 |
| Cu$_2$(CuTCPP) nanosheets | 0.1 | 0.5 | Carbon black/S | 2 | 1.7-2.8 | 1 M LiTFSI in DOL/DME (v/v = 1:1) with 2.0 wt% | 900, 1C, 0.032% | 28 |

LiNO$_3$

| | | | | | | | | |
|---|---|---|---|---|---|---|---|---|
| CNT@ZIF-8 | 0.9 | 15 | Carbon black/S | 1.2 | 1.5-3.0 | 1 M LiTFSI in DOL/DME (v/v = 1:1) with 0.2 M LiNO$_3$ | 100, 0.2C, 0.45% | 29 |
| Ce-MOF/CNT | 0.4 | 8 | Carbon black/S | 2.5 | 1.7-2.8 | 1 M LiTFSI in DOL/DME (v/v = 1:1) with 0.1 M LiNO$_3$ | 800, 1C, 0.022% | 30 |
| MOF@PVDF-HFP | None | 28 | Carbon cloth/S | 1-1.5 | 1.5-3.0 | 1 M LiTFSI in DOL/DME (v/v = 1:1) with 0.1 M LiNO$_3$ | 600, 0.5C, 0.0549% | 31 |
| Bacterial cellulose/2D MOF-Co (BC/2D MOF-Co) | 2.53 | 25 | Carbon black/S | 1.5 | 1.7-2.8 | 1 M LiTFSI in DOL/DME (v/v = 1:1) with 1.0 wt% LiNO$_3$ | 600, 1C, 0.07% | 32 |
| MOF@GO | 0.3 | ~10 | CMK3/S | 0.6-0.8 | 1.5-3.0 | 1 M LiTFSI in DOL/DME (v/v = 1:1) with 0.1 M LiNO$_3$ | 1500, 1C, 0.019% | 33 |

| Laponite nanosheets | 0.7 | 3.5 | Carbon black/S | 1.0-1.2 | 1.7-2.8 | 1 M LiTFSI in DOL/DME (v/v = 1:1) with 0.2 M LiNO$_3$ | 500, 0.2C, 0.06% | 34 |
|---|---|---|---|---|---|---|---|---|
| Ti$_{0.87}$O$_2$ nanosheets | 0.016 | 0.080 | Carbon black/S | 1.5<br>3.5 | 1.7-2.8 | 1 M LiTFSI in DOL/DME (v/v = 1:1) with 1.0 wt% LiNO$_3$ | 5000, 1C, 0.0036%<br>4900, 1C, 0.0035%<br>10000, 2C, 0.0035% | This work |

**Supplementary Table 2.** Comparison of Li$^+$ conductivities of pristine and modified separators.

| Modified separator | Li$^+$ conductivity mS cm$^{-1}$ | Pristine separator | Li$^+$ conductivity mS cm$^{-1}$ | Ref |
|---|---|---|---|---|
| MoS$_2$/Celgard | 0.20 | Celgard | 0.33 | 14 |
| LNS/CB-Celgard | 0.590 | Celgard | 0.559 | 34 |
| MOF@PVDF-HFP | 0.094 | Celgard | 0.138 | 31 |
| MoS$_2$-PDDA/PAA | 0.48 | Celgard | 0.51 | 15 |
| Co-N$_x$@NPC/G-PP | 0.684 | PP | 0.403 | 6 |
| Ti$_{0.87}$O$_2$/PP | 0.381 ± 0.028 | PP | 0.305 ± 0.015 | This work |

## References

[1] Huang, J.-Q. *et al.* Permselective graphene oxide membrane for highly stable and anti-self-discharge lithium-sulfur batteries. *ACS Nano* **9**, 3002–3011 (2015).

[2] Zhuang, T.-Z. *et al.* Rational integration of polypropylene/graphene oxide/nafion as ternary-layered separator to retard the shuttle of polysulfides for lithium-sulfur batteries. *Small* **12**, 381–389 (2016).

[3] Zhou, G. *et al.* A flexible sulfur-graphene-polypropylene separator integrated electrode for ddvanced Li-S batteries. *Adv. Mater.* **27**, 641–647 (2015).

[4] Zhai, P.-Y. *et al.* Scaled-up fabrication of porous-graphene-modified separators for high-capacity lithium-sulfur batteries. *Energy Storage Mater.* **7**, 56–63 (2017).

[5] Pei, F. *et al.* A two-dimensional porous carbon-modified separator for high-energy-density Li-S batteries. *Joule* **2**, 323–336 (2018).

[6] Cheng, Z., Pan, H., Chen, J., Meng, X. & Wang, R. Separator modified by cobalt-embedded carbon nanosheets enabling chemisorption and catalytic effects of polysulfides for high-energy-density lithium-sulfur batteries. *Adv. Energy Mater.* **9**, 1901609 (2019).

[7] Peng, H.-J. *et al.* Janus separator of polypropylene-supported cellular graphene framework for sulfur cathodes with high utilization in lithium-sulfur batteries. *Adv. Sci.* **3**, 1500268 (2016).

[8] Wu, F. *et al.* Light-weight functional layer on a separator as a polysulfide immobilizer to enhance cycling stability for lithium-sulfur batteries. *J. Mater. Chem. A* **4**, 17033–17041 (2016).

[9] Lei, T. *et al.* Inhibiting polysulfide shuttling with a graphene composite separator for highly robust lithium-sulfur batteries. *Joule* **2**, 2091–2104 (2018).

[10] Pang, Y., Wei, J., Wang, Y. & Xia, Y. Synergetic protective effect of the ultralight MWCNTs/NCQDs modified separator for highly stable lithium-sulfur batteries. *Adv. Energy Mater.* **8**,

73

1702288 (2018).

[11] Tu, S. *et al.* A polysulfide-immobilizing polymer retards the shuttling of polysulfide intermediates in lithium-sulfur batteries. *Adv. Mater.* **30**, 1804581 (2018).

[12] Zhou, Y. *et al.* Cationic two-dimensional sheets for an ultralight electrostatic polysulfide trap toward high-performance lithium-sulfur batteries. *Energy Storage Mater.* **9** 39–46 (2017).

[13] Peng, H.-J. *et al.* A Cooperative interface for highly efficient lithium-sulfur batteries. *Adv. Mater.* **28**, 9551–9558 (2016).

[14] Ghazi, Z. A. *et al.* $MoS_2$/Celgard separator as efficient polysulfide barrier for long-life lithium-sulfur batteries. *Adv. Mater.* **29**, 1606817 (2017).

[15] Wu, J. *et al.* Ultralight layer-by-layer self-assembled $MoS_2$-polymer modified separator for simultaneously trapping polysulfides and suppressing lithium dendrites. *Adv. Energy Mater.* **8**, 1802430 (2018).

[16] He, J., Chen, Y. & Manthiram, A. Vertical $Co_9S_8$ hollow nanowall arrays grown on a Celgard separator as a multifunctional polysulfide barrier for high-performance Li-S batteries. *Energy Environ. Sci.* **11**, 2560–2568 (2018).

[17] Tian, Y. *et al.* Low-bandgap se-deficient antimony selenide as a multifunctional polysulfide barrier toward high-performance lithium-sulfur batteries. *Adv. Mater.* **32**, 1904876 (2020).

[18] Li, M. *et al.* A separator-based lithium polysulfide recirculator for high-loading and high-performance Li-S batteries. *J. Mater. Chem. A* **6**, 5862–5869 (2018).

[19] Song, J. *et al.* Immobilizing polysulfides with MXene-functionalized separators for stable lithium-sulfur batteries. *ACS Appl. Mater. Interfaces* **8**, 29427–29433 (2016).

[20] Sun, J. *et al.* Entrapment of polysulfides by a black-phosphorus-modified separator for lithium-

sulfur batteries. *Adv. Mater.* **28**, 9797–9803 (2016).

[21] Wang, Z. *et al.* Constructing metal-free and cost-effective multifunctional separator for high-performance lithium-sulfur batteries. *Nano Energy* **59**, 390–398 (2019).

[22] Kim, P. J. H. *et al.* Synergistic protective effect of a BN-carbon separator for highly stable lithium sulfur batteries. *NPG Asia Mater.* **9**, e375 (2017).

[23] Yim, T. *et al.* Effective polysulfide rejection by dipole-aligned $BaTiO_3$ coated separator in lithium–sulfur batteries. *Adv. Funct. Mater.* **26**, 7817–7823 (2016).

[24] Lu, Q. *et al.* An "electronegative" bifunctional coating layer: simultaneous regulation of polysulfide and Li-ion adsorption sites for long-cycling and "dendrite-free" Li-S batteries. *J. Mater. Chem. A* **7**, 22463–22474 (2019).

[25] Xiao, Z. *et al.* A lightweight $TiO_2$/graphene interlayer, applied as a highly effective polysulfide absorbent for fast, long-life lithium-sulfur batteries. *Adv. Mater.* **27**, 2891–2898 (2015).

[26] Zhao Y. *et al.* Dense coating of $Li_4Ti_5O_{12}$ and graphene mixture on the separator to produce long cycle life of lithium-sulfur battery. *Nano Energy* **30**, 1–8 (2016).

[27] Zang, Y. *et al.* Large-area preparation of crack-free crystalline microporous conductive membrane to upgrade high energy lithium-sulfur batteries. *Adv. Energy Mater.* **8**, 1802052 (2018).

[28] Tian, M. *et al.* Ultrathin MOF nanosheet assembled highly oriented microporous membrane as an interlayer for lithium-sulfur batteries. *Energy Storage Mater.* **21**, 14–21 (2019).

[29] Wu, F. *et al.* Metal-organic frameworks composites threaded on the CNT knitted separator for suppressing the shuttle effect of lithium sulfur batteries. *Energy Storage Mater.* **14**, 383–391 (2018).

[30] Hong, X.-J. *et al.* Cerium based metal-organic frameworks as an efficient separator coating catalyzing the conversion of polysulfides for high performance lithium–sulfur batteries. *ACS Nano* **13**,

1923–1931 (2019).

[31] He, Y. *et al.* Simultaneously inhibiting lithium dendrites growth and polysulfides shuttle by a flexible MOF-based membrane in Li-S batteries. *Adv. Energy Mater.* **8**, 1802130 (2018).

[32] Li, Y. *et al.* Single atom array mimic on ultrathin MOF nanosheets boosts the safety and life of lithium-sulfur batteries. *Adv. Mater.* **32**, 1906722 (2020).

[33] Bai, S., Liu, X., Zhu, K., Wu, S. & Zhou, H. Metal-organic framework-based separator for lithium-sulfur batteries. *Nat. Energy* **1**, 16094 (2016).

[34] Yang, Y. & Zhang, J. Highly stable lithium-sulfur batteries based on laponite nanosheet-coated celgard separators. *Adv. Energy Mater.* **8**, 1801778 (2018).